Ore Geology Reviews 86 (2017) 459–473

Contents lists available at ScienceDirect

Ore Geology Reviews

journal homepage: www.elsevier.com/locate/oregeo

Fluid and metal sources of the Wenquan porphyry molybdenum deposit, Western Qinling, NW China

Kun-Feng Qiu [a,b,c,*], Erin Marsh [b], Hao-Cheng Yu [a], Katharina Pfaff [d], Cayce Gulbransen [b], Zong-Yang Gou [a], Nan Li [a]

[a] State Key Laboratory of Geological Processes and Mineral Resources, China University of Geosciences, Beijing 100083, China
[b] U.S. Geological Survey, Box 25046, Mail Stop 973, Denver Federal Centre, Denver, CO 80225-0046, USA
[c] Key Laboratory of Western Mineral Resources and Geological Engineering of Ministry of Education, Chang'an University, Xi'an 710054, China
[d] Department of Geology and Geological Engineering, Colorado School of Mines, Golden, CO 80401, USA

ARTICLE INFO

Article history:
Received 26 November 2016
Received in revised form 24 February 2017
Accepted 28 February 2017
Available online 1 March 2017

Keywords:
Microthermometry
H-O-S-Fe isotopes
Fluid and metal sources
Wenquan porphyry deposit
Western Qinling

ABSTRACT

The Wenquan porphyry moybdenium deposit, Western Qinling, NW China, with a resource of 247 million tonnes at 0.048% Mo, formed during Triassic collision between South China and North China blocks. Ore fluids at Wenquan vary widely in composition from single-phase, low-salinity aqueous to low-salinity vapor, and hypersaline inclusions. Fluid inclusion assemblages in a quartz-molybdenite vein contain >60 vol% vapor, are equant to negative-crystal shaped, and form clusters or distinct inclusion trails. They yield homogenization temperatures of 285–295 °C, with an estimated trapping temperature of 425 °C, suggesting a paleodepth of about 5 km calculated at a pressure correction of 100–150 MPa. Hydrothermal K-feldspar from early stockwork veins related to potassic alteration have calculated $\delta^{18}O_{fluid}$ values of −1.9‰ to +1.9‰. Hydrothermal sericite from an overprinting phyllic alteration associated with late quartz-pyrite veins has calculated δD_{fluid} values between −68 and −60‰, and $\delta^{18}O_{fluid}$ values from −3.7 to +1.4‰. These isotopic data suggest that both early- and late-stage fluids are dominated by magmatic fluids, with influx of meteoric water during the late stage. Exsolution of volatiles from magma in a late-stage open system, results in more variable δD values than an earlier closed-system.

Molybdenite and pyrite have $\delta^{34}S$ values ranging from 1.1‰ to 6.6‰, indicating that sulfur at Wenquan had a magmatic source. A linear relationship between $\delta^{34}S$ values of sulfides separated from early potassic alteration and late phyllic alteration could reflect incorporation of isotopically heavy evaporate sulfate into source magmas from underlying Devonian sedimentary rocks during late alteration. The $\delta^{56}Fe$ whole-rock values of altered porphyries range from 0.08‰ to 0.26‰, similar to $\delta^{56}Fe$ values of 0.15‰–0.32‰ for pyrite from quartz veins related to both the potassic and phyllic alteration assemblages. The $\delta^{56}Fe$ values of pyrite are positively correlated to, but in general slightly lighter than, those of altered porphyries, indicating similar metal sources. Moreover, both altered porphyries and the pyrite are progressively enriched in heavy Fe isotopes from biotite, through potassic to late phyllic alteration, consistent with isotopic evolution from an early lithostatic load to a late hydrostatic load.

The Triassic intrusive rocks and fluids responsible for mineralization were derived from a deeply-sourced hybrid mantle-crustal magma crystallizing at a paleodepth of 5 km under lithostatic load. External Late Triassic meteoric or Devonian formational fluids became a part of the hydrothermal system during the post-fracturing final stage of ore formation under a hydrostatic regime. The formation of the Wenquan magmatic-hydrothermal systems spans the ductile-brittle transition based on a normal thermal gradient as constrained by the temperature range of 550–300 °C. The early, high-temperature potassic alteration developed under a ductile regime, whereas the later, low-temperature phyllic alteration correlates to a brittle environment, where hydraulic rock fracturing enhances permeability and fluid circulation. Most sulfur and metals were precipitated from vapor-rich fluids resulting from cooling and expansion of a single-phase fluid exsolved from a hybrid magma.

* Corresponding author at: State Key Laboratory of Geological Processes and Mineral Resources, China University of Geosciences, Beijing 100083, China.
E-mail addresses: kunfengqiu@qq.com, kunfengqiu@gmail.com (K.-F. Qiu).

http://dx.doi.org/10.1016/j.oregeorev.2017.02.035
0169-1368/

1. Introduction

The Central China Orogenic Belt, consisting of the Kunlun, Qilian, Qinling and Dabie Mountains from west to east, is located in central Eastern Asia, and formed during ocean basin closures and subsequent collision between the North China Block and Tarim Block to the north, and South China Block and Tibet to the south (Fig. 1A, Meng and Zhang, 2000; Deng et al., 2013; Pirajno and Zhou, 2015). The Qinling Orogenic Belt, linking the Kunlun and Qilian Mountains in the west and the Dabie Mountain to the east, is separated into the Western Qinling and Eastern Qinling segments (shown as blue dashed line in Fig. 1B; Zhang et al., 2007; Liu et al., 2010; Tang et al., 2015), on the basis of regional geology and lithospheric features defined by geophysical studies. Several studies have reviewed the evolution of the Qinling Orogen that culminated with collision between the North China and South China Blocks (Chen and Santosh, 2014; Dong and Santosh, 2016). Eastern Qinling is well endowed with porphyry Mo deposits, with a proven and inferred resource exceeding 6 million tonnes (Mt) Mo metal (Mao et al., 2008; Li et al., 2013). In contrast, porphyry systems in Western Qinling have been poorly documented, although they were first recognized as early as the 1970s (GSBGME, 1979; Xiang et al., 1985) and now comprise dozens of porphyry and associated skarn deposits (Fig. 1B; Qiu et al., 2016; Qiu and Deng, 2016 and references therein). These include the Jiangligou W-Mo, Xiekeng, Nianmuer Cu-As-Au, Amangshaji Cu, Longdegang Cu-As, Zaozigou Au, Dewulu Cu, Nanban Cu, Laodou Au-Cu, Riduoma Fe, Xiahejiangang Fe, Shanglanggang Fe, Wenquan Mo, and Taiyang-

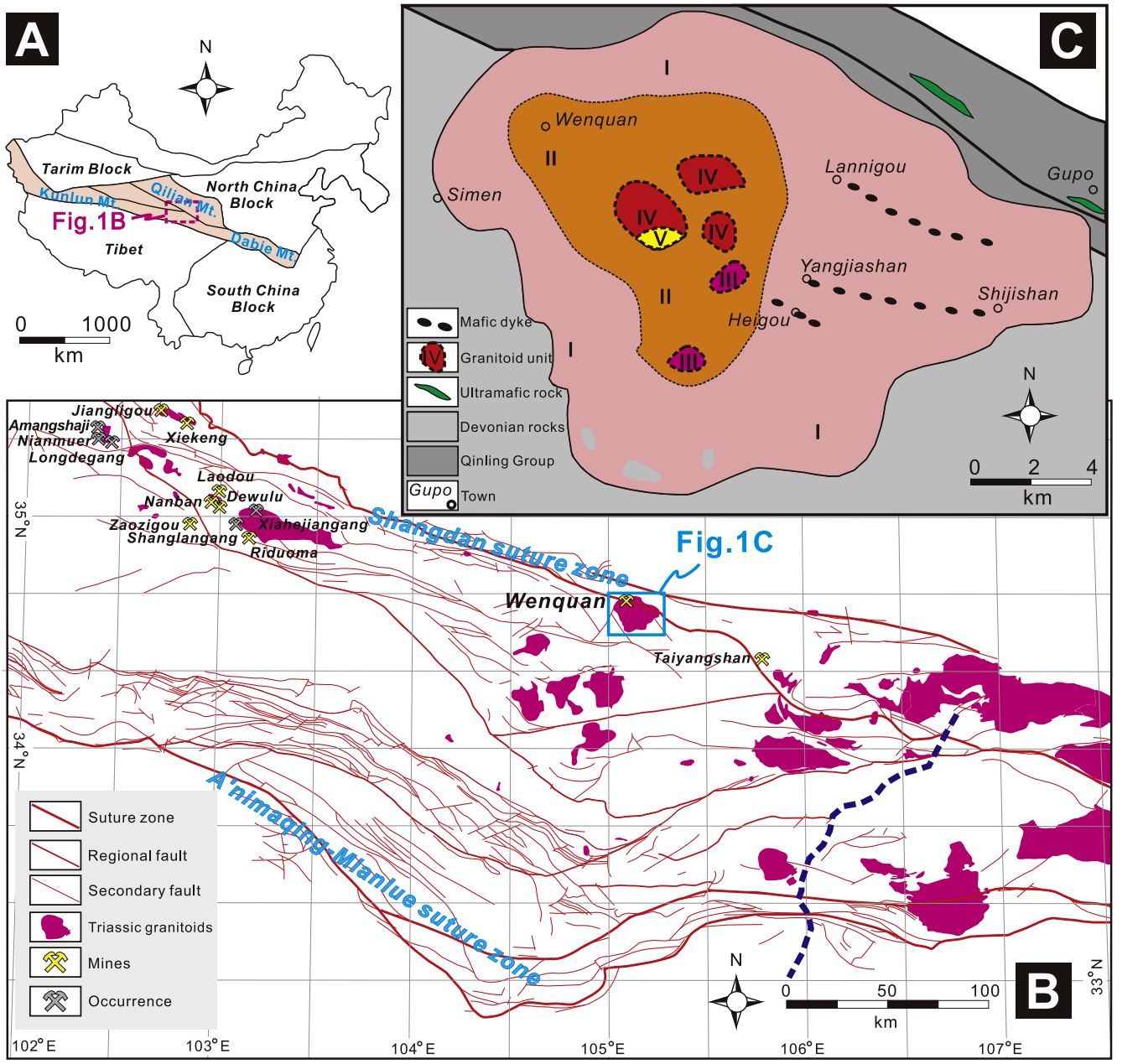

Fig. 1. (A) Tectonic subdivision of China, showing the location of Western Qinling. (B) Generalized geological map of Western Qinling, showing major Triassic porphyry-skarn systems and distribution of their associated granites (modified after Meng and Zhang, 2000; Yang et al., 2015a). (C) Sketch geological map of the Wenquan area, showing the five phases: biotite granite (I), biotite monzogranite porphyry (II), porphyritic monzogranite (III), monzogranite porphyry (IV), and porphyritic syenogranite (V) of the composite Wenquan granite batholiths (Modified after Han, 2009; Wang, 2011 and this field investigation).

shan Cu deposits. Ore genesis studies using modern methodologies on select deposits, as well as reconstructions of the regional structural and tectonic setting for the porphyry magmatism, are critically needed to increase targeting strategies for exploration in Western Qinling.

Besides the world-famous Late Mesozoic (Late Jurassic–Early Cretaceous) porphyry Mo systems located in the Eastern Qinling, Early Mesozoic (mainly Triassic) Mo deposits throughout the Qinling Orogen have been discovered and recognized (Li and Pirajno, 2017). Wenquan, the only large Triassic porphyry Mo deposit in the Western Qinling, however formed by fluids with different characteristics compared to fluids that formed coeval porphyry Mo deposits in Eastern Qinling (Ren, 2009; He, 2012; Chen et al., 2017). The Wenquan Mo deposit is easily accessible and has well-developed alteration zonation, distinct mineralization styles, and clear mineral assemblages, making it amenable to a comprehensive ore genesis study. The Wenquan deposit comprises 247 Mt ore in the measured and indicated categories, and 0.12 Mt Mo metal at a grade of 0.048% Mo (He, 2012). Previous robust Re–Os dating on molybdenite from quartz-molybdenite veins, and numerous geochronological and geochemical studies on the associated granitoids, combined with geological investigations, have provided a basic framework for the geological environment and outlined possible genetic relationships at Wenquan (e.g., Han, 2009; Zhu et al., 2011). However, there remains no consensus on a holistic genetic model for ore formation at Wenquan. The key to understanding the uncertainties in ore genesis lies in defining the nature of the ore fluids and metal sources for the deposit.

Four types of fluid inclusions have been recognized in the Wenquan deposit based on detailed petrography (Han, 2009; Ren, 2009; He, 2012; Wang et al., 2012): single-phase aqueous inclusions, vapor-rich fluid inclusions, hypersaline liquid inclusions, and low-salinity aqueous inclusions. However, no specific geological information was provided to illustrate which of the multi-generations of quartz in a complex paragenetic sequence was chosen for fluid inclusion analyses in the past research. Moreover, most microthermometric data recorded from these previous studies were not collected following the procedure by Goldstein and Reynolds (1994) of defining Fluid Inclusion Assemblages that carefully discriminated groups of petrographically associated fluid inclusions trapped at the same time and conditions, which is essential for identifying post-entrapment modification of fluid inclusions from necking down, stretching, or leakage and refilling (Bodnar, 2003). Measurements of ice-melting temperature (Tm, ice), halite dissolution temperature (Ts, halite), and homogenization temperatures of fluid phases in these fluid inclusions (Th, total) thus inevitably provide little accurate information about ore fluid characteristics at the pressure and temperature of entrapment of the fluids.

Stable isotope geochemistry is typically applied to furnish invaluable information concerning the genesis and physiochemical aspects of ore-forming hydrothermal solutions, as well as to constrain the origin and evolution of some ore-forming components (Calagari, 2003; Goldfarb and Groves, 2015). Some workers reported hydrogen and oxygen isotopic compositions ($\delta D = -96$ to $-68‰$; $\delta^{18}O_{fluid} = -0.9$ to $+0.6‰$) from inclusion fluids extracted from quartz grains separated from quartz-molybdenite veins at the Wenquan deposit, and proposed that the ore fluids were a mixture of magmatic and meteoric waters (Han, 2009; Ren, 2009; He, 2012). Fluid inclusions in quartz, a ubiquitous gangue mineral of hydrothermal deposits, have long been extensively used to define fluid sources. Scanning electron microscope and cathodoluminescence (CL) techniques, however, have confirmed that early-formed quartz grains are readily overprinted by later hydrothermal events, and these techniques define different generations not observed under an optical microscope (Rusk et al., 2006, 2008; Qiu et al., 2015). This observation indicates that the quartz that has been overprinted could host fluid inclusions correlated to multiple hydrothermal events. The isotopic data collected from such quartz and trapped fluid inclusions therefore cannot be used to interpret the formation of the ore deposit.

Han (2009) and He (2012) measured sulfur isotopes on molybdenite ($\delta^{34}S = +4.69$ to $+6.61‰$) separated from quartz-molybdenite veins, and proposed that sulfur was sourced from the lower crust and upper mantle. Wang (2011) and Zhu et al. (2011) reported sulfur isotopic values of pyrite ($\delta^{34}S = +5.02$ to $+5.58‰$) and molybdenite ($\delta^{34}S = +5.46$ to $+5.66‰$) from quartz-sulfide veins, and suggest that magmatic-hydrothermal fluids associated with granitoids were the major sulfur source at Wenquan. They suggested that mineralization resulted from internal fractional crystallization of fluids within the Triassic magmatic system. However, the lack of detailed paragenetic information on these sulfides hinders interpretation. Pyrite occurs as a ubiquitous mineral in different quartz-sulfide veins at Wenquan (Zhu et al., 2011; Qiu et al., 2015), so only pyrite that can be clearly ascribed to a specific stage can provide meaningful genetic information.

The principal aim of this study is to elucidate the source and evolution of fluids and metals for porphyry mineralization in order to provide a comprehensive ore genesis model for the Wenquan mineral system. Previous research at Wenquan has provided a geologic framework for geodynamic setting, the duration of magmatic-hydrothermal processes, and the nature of alteration zonation and mineralization styles. This previous work has been enhanced here through drill core logging and new fieldwork. We present carefully constrained fluid-inclusion microthermometric data for least-overprinted quartz samples following careful petrography using the Goldstein and Reynolds (1994) approach, in concert with SEM and CL imaging. Furthermore, stable isotope geochemistry is presented for minerals of different well-defined mineralization and alteration generations.

2. Geological background

2.1. Regional geology

The Triassic Western Qinling Orogenic Belt is an important geological boundary that separates the North and South China Blocks. This belt is tectonically bounded by the North China Block and Qilian Mountain Terrane to the north of the Shangdan suture zone (Fig. 1B), and A'nimaqing-Mianlue suture zone (Fig. 1B; Deng et al., 2014b; Dong et al., 2016; Wang et al., 2016a), which defines the eastern branch of Paleotethys Ocean, to the south (Bian et al., 2004; Wang et al., 2014; Deng et al., 2014a). The Paleozoic Shangdan suture zone reflects closure of the Shangdan Ocean and multistage amalgamation of the South China Block-South Qinling Block to the North China Block during the Paleozoic (Meng and Zhang, 2000; Yang et al., 2015b; Tang et al., 2016). This suture zone comprises discontinuously exposed mélange, mainly Paleozoic ophiolitic assemblages, and subduction-related volcanic and sedimentary rocks, all intensely deformed during Paleozoic thrusting, Late Triassic sinistral ductile-shearing, and Cretaceous brittle faulting (Ratschbacher et al., 2003; Li et al., 2014; Liu et al., 2015). The Triassic A'nimaqing-Mainlue suture zone represents the closure of a northern branch of the eastern Paeotethyan Ocean which separated the South Qinling Block from the South China Block (Chen and Santosh, 2014). The suture zone is characterized by intensively dismembered ophiolite and arc-related volcanic rocks, high-pressure/temperature metamorphic rocks, and continental-margin sedimentary rocks of Paleozoic to Middle Triassic age. These were later affected by south-directed overthrusting during the Late Jurassic to Cretaceous (Dong and Santosh, 2016).

The Triassic Western Qinling Orogenic Belt underwent a multi-stage amalgamation process between the South and North China Blocks, from the Proterozoic up to late Mesozoic (Dong et al., 2016). The widely-exposed Devonian to Middle Triassic sedimentary rocks record deformation related to this subduction and collision history, whereas the Precambrian basement rocks are rarely exposed (Luo et al., 2012). Mesozoic magmatism is widespread in Western Qinling, with hundreds of Triassic granitic plutons intruded throughout the belt between the Paleozoic Shangdan and Triassic A'nimaqing-Mianlue suture zones (Li et al., 2013; Wang et al., 2013; Deng and Wang, 2016). Subsequent uplift and exhumation led to the widespread exposure of Triassic granitoids in the belt (Chen and Santosh, 2014), with closely-related porphyry-skarn deposits (Qiu et al., 2015; Qiu and Deng, 2016 and references therein).

2.2. Geology of the Wenquan deposit

The Wenquan porphyry Mo deposit is hosted in the Wenquan batholith (E105°04′–E105°08′, N34°35′–N34°38′), which is irregular in shape, and covers an area of about 250 km^2 (Fig. 1B). The Wenquan batholith consists of five units: biotite granite, biotite monzogranite porphyry, porphyritic monzogranite, monzogranite porphyry, and porphyritic syenogranite (Fig. 1C; Han, 2009). In the northeast, the composite batholith intruded a suite of gently-dipping strata of the Paleoproterozoic to Mesoproterozoic Qinling Group, consisting predominantly of schist and gneiss, and the Devonian Dacaotan Group, primarily composed of clastic and carbonate rocks in the southwest (Qiu et al., 2014). Three NW-trending mafic dikes named Lannigou (~8 km), Yangjiashan-Shijishan (~8 km) and Heigou (~4 km) intrude the batholith to the northeast (Han, 2009). Abundant mafic enclaves are hosted mainly by biotite monzogranite porphyry, porphyritic monzogranite, and monzogranite porphyry (Fig. 1C; Cao et al., 2011; Qiu et al., 2014). These mafic enclaves show consistent directional alignment as well as mineral assemblages and geochemical composition to that of mafic dikes (Han, 2009; Zhu et al., 2011).

The host granite porphyries of the Wenquan complex batholith are an intermediate to felsic, and high-K calc-alkaline to shoshonitic suite of peraluminous to metaluminous granites with I-type affinity (Zhu et al., 2011). They have relatively higher MgO contents and $Mg^{\#}$ compared to normal crustal-derived felsic magmas, but lower Nb/Ta ratios compared to the mafic enclaves (Cao et al., 2011; Zhu et al., 2011). These hybrid magmas resulted from magma mixing during their Late Triassic emplacement at roughly the transition from a collisional setting, between the South Qinling and South China Blocks, to a post-collision setting (Zhu et al., 2011; Chen and Santosh, 2014). At the Wenquan deposit, biotite granite porphyry and monzogranite porphyry are the two prominent phases associated with Mo mineralization (Fig. 2).

Uranium–lead ages on zircons from these ore-hosting granites are reported as 223 ± 3 Ma and 225 ± 3 Ma (Cao et al., 2011), 218 ± 2.4 Ma and 221 ± 1.3 Ma (Xiong et al., 2016), and 217.2 ± 2.0 Ma and 216.2 ± 1.7 Ma (Wang, 2011; Zhu et al., 2011), respectively. The mafic enclaves hosted in the porphyries yield zircon U–Pb ages of 217 ± 2.0 Ma and 218 ± 2.5 Ma (Xiong et al., 2016), respectively. Zircons from host porphyries have negative $\varepsilon_{Hf}(t)$ values of −3.6 to −0.1, with two-stage Hf model ages (T_{DM2}) of 1056–1234 Ma, and positive $\varepsilon_{Hf}(t)$ values ranging from +0.1 to +3.0, with single-stage Hf model ages (T_{DM1}) of 739–868 Ma (Wang, 2011; Xiong et al., 2016). This indicates that the host porphyries are most likely formed by partial melting of Mesoproterozoic lower continental crust. Zircons in the mafic enclaves have negative $\varepsilon_{Hf}(t)$ values ranging from −10.1 to −0.1 and T_{DM2} of 1052–1565 Ma, and have positive $\varepsilon_{Hf}(t)$ values of +0.5 to +10.8 and corresponding T_{DM1} of 441–856 Ma (Zhu et al., 2011; Xiong et al., 2016), suggesting an origin by partial melting of Neoproterozoic subcontinental lithosphere mantle.

Alteration zones at Wenquan are well developed outward from a potassic, to phyllic, and then to propylitic silicate + sulfide + oxide assemblage (Fig. 2A; Han, 2009). Porphyry-style Mo mineralization at Wenquan consists predominantly of stockworks, veinlets, and disseminated sulfides (Fig. 3). The NS-trending orebodies comprise planar to irregular veins that dip 30° to 75° northeast (Fig. 2B, Han, 2009). The disseminated Mo mineralization is generally developed within the biotite granite porphyry and monzogranite porphyry bodies, which contain widespread mafic enclaves. Previous Re–Os dating on molybdenite from quartz-molybdenite veins yielded model ages of 214.4 ± 7.1 Ma (Song et al., 2008; Zhu et al., 2009) and 219 ± 5.2 Ma (Xiong et al., 2016). The molybdenite from quartz-molybdenite veins has Re contents of 20–33 μg/g, suggesting mantle involvement for the magma and metal source (Song et al., 2008; Zhu et al., 2009).

3. Samples and analytical methods

3.1. Optical and QEMSCAN microscopy

All 53 samples collected from the Wenquan deposit were preliminarily surveyed by transmitted and reflected microscopy, and then seven selected samples were analysed using automated scanning electron microscopy (QEMSCAN) at the Colorado School of Mines to more comprehensively determine mineral assemblages. The samples were loaded into the QEMSCAN instrument and analyses were initiated using the control program (iDiscover, FEI). Four energy dispersive X-ray (EDX) spectrometers acquired spectra from each particle with a beam stepping interval (i.e., spacing between acquisition points) of 20 μm, an accelerating voltage of 25 keV, and a beam current of 5 nA. Interactions between the beam and the sample were modeled through Monte Carlo simulation. The EDX spectra were compared with known spectra allowing an assignment to be made of a composition at each acquisition point. The assignment makes no distinction between mineral species and amorphous grains of similar composition. Results were output by the QEMSCAN software as a spreadsheet giving the area percent of each composition in the pre-existing spectra. This procedure allows a compositional map of each sample to be generated. Composition assignments were grouped appropriately.

3.2. Fluid inclusion petrography

Reconnaissance fluid-inclusion petrography was conducted on quartz veins from all paragenetic stages recognized by observing intersection and overprinting relationships between different veins (veinlets), intrusive contacts, and alteration types (halos) and temporal-spatial relationships of gangue and ore minerals by using microscope and QEMSCAN. Subsequently, optical microscopy and detailed fluid inclusion petrography were performed at the U.S. Geological Survey in Denver on selected quartz vein samples with an Olympus BX51 microscope using a series of doubly polished, 60 μm-thick sections. Microthermometric data on selected fluid inclusions were collected using a Fluid Inc.-adapted U.S. Geological Survey gas-flow heating and freezing stage that was calibrated using synthetic fluid inclusions. Freezing temperatures were accurate to ±0.1 °C. The accuracy of heating measurements ranged from approximately ±2 °C at 200 °C to approximately ±10 °C at temperatures above 600 °C. Imaging of representative fluid inclusions was conducted using an OptronicsMicrofire A/R camera at the Colorado School of Mines.

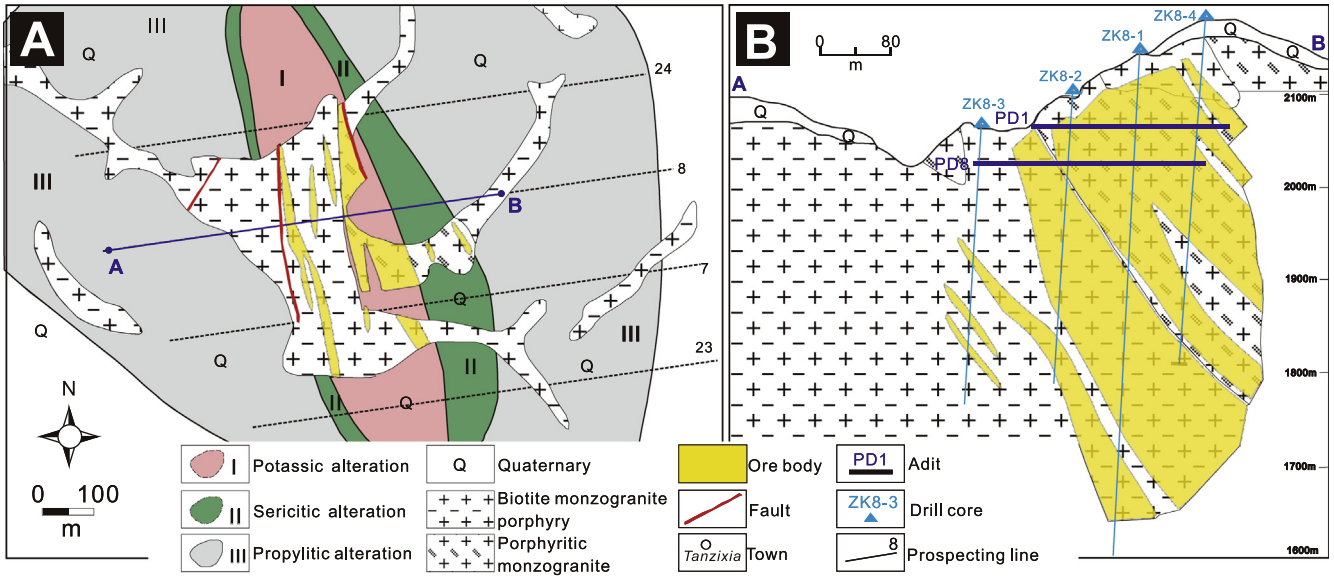

Fig. 2. (A) Generalized geological map of the Wenquan porphyry Mo deposit illustrating principal geology and alteration zonings. (B) Profile of diamond drill core section through Line A-B in Figure A.

3.3. Hydrogen and oxygen isotopes

Oxygen and hydrogen isotope analyses were conducted on ore-related sericite separates from quartz-pyrite-sericite phyllic assemblage veins. Additional oxygen isotope analyses were performed on K-feldspar separates from the potassic halos surrounding quartz-chalcopyrite-pyrite-molybdenite veins and quartz-molybdenite-chalcopyrite veins truncated by late quartz-pyrite-sericite veins. Pure sericite aggregates and K-feldspar flakes were obtained by crushing, washing and drying, and then hand-picking using a binocular microscope. The isotopes were measured in the Isotope Laboratory at the U.S. Geological Survey in Denver. Oxygen was extracted from 15 to 20 mg silicate minerals by reaction with BrF_5 and then reacted with carbon to give CO_2 (Clayton and Mayeda, 1963), whereas hydrogen was liberated as water by the fusion of the samples and then reacted with zinc to give H_2 (Coleman et al., 1982). The resultant CO_2 was analysed for oxygen isotopes using a Finnigan MAT-252 mass spectrometer, whereas the hydrogen isotopes were obtained using a MAT 253. The precisions for O and H isotopes are ±0.1 and ±2 per mil (1σ), respectively. The $^{18}O/^{16}O$ and D/H ratios are reported in normal δ-notation relative to V-SMOW standard. Hydrogen isotopic compositions of ore fluids (δD_{fluid}) in equilibrium with the hydrothermal sericite were calculated using the sericite-water equilibrium function of Marumo et al. (1980): $\delta D_{fluid} = \delta D_{mineral} + 22.1 \times 10^6\, T^{-2} - 19.1$. Oxygen isotopic compositions of ore fluids ($\delta^{18}O_{fluid}$) were calculated using the K-feldspar-water equations ($\delta^{18}O_{fluid} = \delta^{18}O_{mineral} - 2.91 \times 10^6 T^{-2} + 3.41$), and muscovite-water fractionation factors ($\delta^{18}O_{fluid} = \delta^{18}O_{mineral} - 2.38 \times 10^6 T^{-2} - 3.89$) of Zheng (1993).

3.4. Sulfur isotopes

Sulfur isotope measurements were collected for sulfide minerals separated from quartz-sulfide veins in the Isotope Laboratory at the U.S. Geological Survey in Denver. Mineral separations using standard methods of concentration were performed by conventional preparation techniques including crushing, heavy liquids, and magnetic separation. Prior to subsequent preparation for isotopic analyses, the purity of all concentrates was checked by examination under a binocular microscope to ensure they were not oxidized, and contaminant-free, and thus essentially monomineralic. Purities were 95% to, more commonly, 99% or better. Aliquots of pyrite and molybdenite were combined with V_2O_5 and combusted in an elemental analyzer. Sulfur isotope ratios were determined by an on-line method using an elemental analyzer coupled to a Micromass Optima mass spectrometer (Giesemann et al., 1994). Analytical results are generally reproducible within ±0.2 per mil (2σ). Isotope data are reported in conventional δ notation relative to the Canyon Diablo Troilite (CDT) standard. The measured and calculated oxygen and hydrogen isotopic compositions are listed in Table 1. Sulfur isotope data in this study and previous literature are summarized in Table 2.

3.5. Iron isotopes

Iron isotopic analyses were conducted on pyrite separates (B01, C01, C02, D01 and E01) and altered monzogranite porphyry samples (B02, C03, D02, E02 and E03) that are cut by quartz-sulfide veins (Fig. 3). Sample W31 is altered with hydrothermal biotite and crosscut by a quartz-chalcopyrite-pyrite vein (Fig. 3B). Sample W32 is potassically altered and crosscut by a quartz-chalcopyrite-pyrite-molybdenite vein (Fig. 3C). Sample W33 represents potassically altered rock crosscut by a quartz-molybdenite-pyrite vein (Fig. 3D), whereas Sample W34 is characterized by sericitic selvages along a quartz-pyrite-sericite vein within an area of potassic alteration (Fig. 3E). The Fe isotopic compositions of granitoid samples and pyrite separates from the Wenquan deposit are presented in Table 3.

Iron isotopic analyses were conducted in the Isotope Geochemistry Laboratory at the China University of Geosciences, Beijing (CUGB). The analytical procedures were previously reported by He et al. (2015). Bulk samples were carefully cleaned ultrasonically in purified Elga H_2O (18.2 MΩ) before crushing and milling into minus-200 mesh powders. Approximately 30 mg of whole-rock powder was dissolved with a concentrated in a HF-HNO_3-$HClO_4$ mixture, whereas pyrite separates were dissolved using a concentrated HF-HNO_3-HCl mixture at 130 °C. Sample solutions were then evaporated to dryness after complete dissolution, and refluxed with aqua regia (HCl:HNO_3 = 3:1) and excess HNO_3 aqua regia (HCl:HNO_3 = 2:1) successively at 130 °C. The solutions were

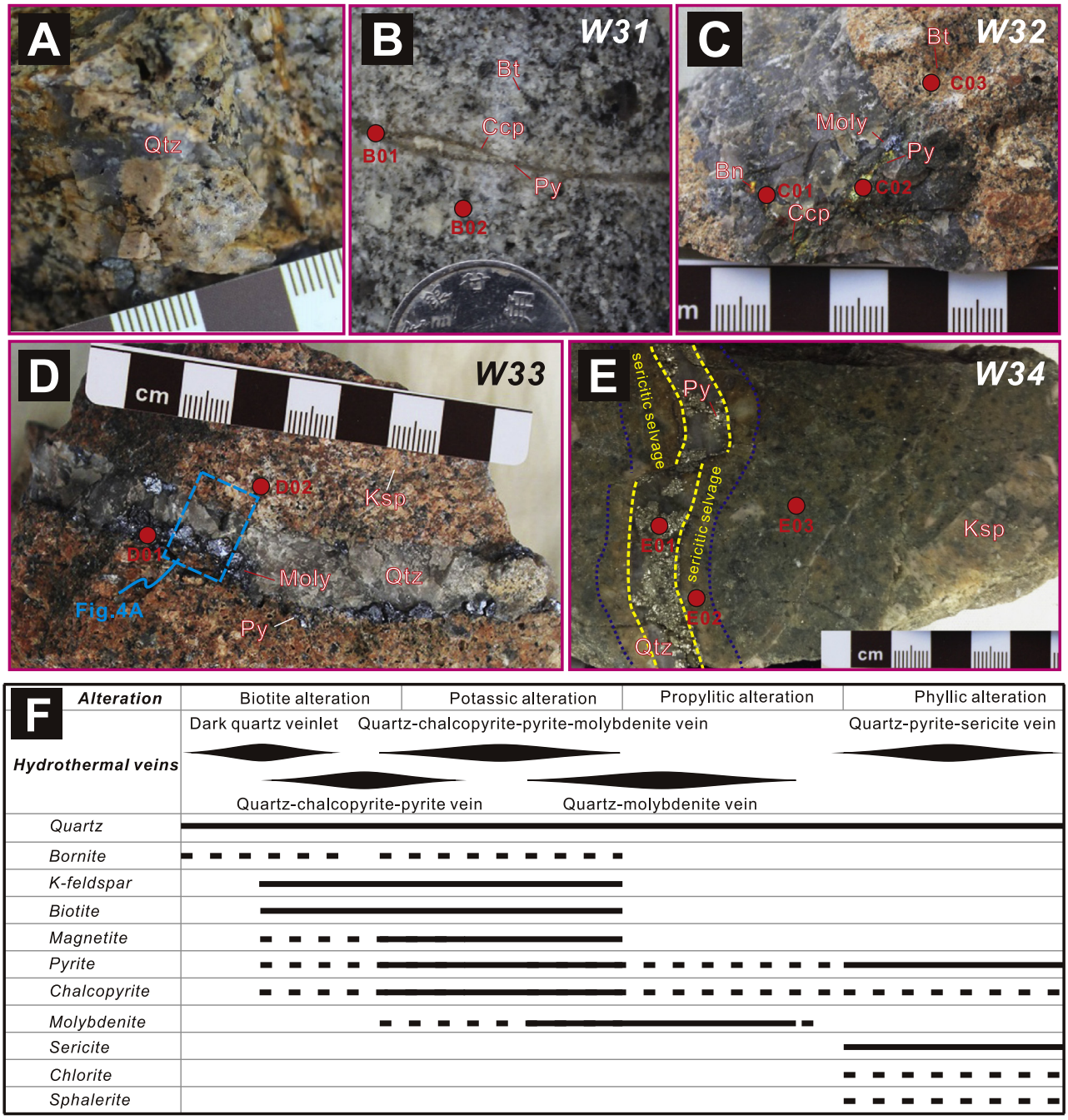

Fig. 3. Photographs of quartz stockwork veins at Wenquan. (A) The barren early irregular, discontinuous, and segmented dark-quartz veinlets. (B) The quartz-chalcopyrite-pyrite veins with mineral assemblage of quartz, K-feldspar, biotite, magnetite and minor pyrite, generally associated with biotite alteration. (C) The quartz-chalcopyrite-pyrite-molybdenite veins, consisting of quartz, K-feldspar, biotite, magnetite and chalcopyrite, with minor pyrite, molybdenite and bornite. (D) The quartz-molybdenite vein, with mineral assemblage of quartz and molybdenite, with minor pyrite and chalcopyrite. (E) The quartz-pyrite-sericite vein, filled predominantly with mineral assemblage of quartz, pyrite, sericite, chlorite and lesser sphalerite. (F) The silicate, sulfide and oxide assemblages in hydrothermal quartz vein sequences showing ore and gangue mineral paragenesis and their associated alteration types. The following mineral abbreviations are from Whitney and Evans (2010): Bn = bornite, Bt = biotite, Ccp = chalcopyrite, Chl = chlorite, K-spar = K-feldspar, Mag = magnetite, Moly = molybdenite, Py = pyrite, Qtz = quartz, Ser = sericite, Sph = sphalerite. The black full lines indicate high abundance and the black dashed lines represent minor amounts in the paragenetic sequence box.

subsequently evaporated to dryness at 100 °C. Finally, residues were dissolved in 6 N HCl for chromatographic purification. Iron was separated from matrix elements and potential isobars with AG1X-8 resin (200–400 mesh) in a HCl medium. Isotopic ratios were analysed by the sample-standard bracketing method using a Thermo-Finnigan Neptune Plus MC-ICPMS on high resolution modes. The measurement sequence was repeated four times to get better reproducibility and accuracy, and the data are reported in the traditional δ values relative to IRMM-014 ($\delta^{i}Fe = [(^{i}Fe/^{54}Fe)_{sample}/(^{i}Fe/^{54}Fe)_{IRMM\text{-}014}-1] \times 1000$, where i can be 56 or 57). Internal errors are reported as 2se, 95% confidence interval after Dauphas et al. (2004) and He et al. (2015). The long-term external reproducibility and accuracy on $\delta^{56}Fe$ are estimated to be better than ±0.05‰ (2SD) (He et al., 2015). Geostandard GSP-2 (granodiorite) and BCR-2 (basalt) were processed during the course of this study.

Table 1
Hydrogen and oxygen isotopic compositions of K-feldspar and sericite separates at Wenquan.

Sample description	Mineral	$\delta^{18}O_{mineral}$(‰)	$\delta D(‰)_{SMOW}$	T (°C)	$\delta^{18}O_{fluid}$(‰)	δD_{fluid}(‰)
Potassic halo along Qtz-Ccp-Py vein	K-feldspar	2.8		550	1.9	−45
Qtz-Py-Ser vein	Sericite		−99	300	−3.4	−51
Qtz-Py-Ser vein	Sericite	3.6	−98	300	0.3	−50
Qtz-Py-Ser vein	Sericite		−105	300	−3.4	−57
Potassic halo along Qtz-Moly-Ccp vein	K-feldspar	0.6		425	−1.9	−45
Qtz-Py-Ser vein	Sericite	−1.4	−103	300	−4.8	−54
Potassic halo along Qtz-Moly-Ccp vein	K-feldspar	1.4		425	−1.2	−45

Table 2
Sulphur isotopic compositions ($\delta^{34}S$‰) of sulfides at Wenquan.

Sample No.	Silicate + sulfide + oxide assemblage	Mineral	$\delta^{34}S$ (‰)
WQ13S12	Qtz + K-spar + Bt + Mag + Ccp ± Py	Py	1.1
WQ13S11	Qtz + K-spar + Bt + Mag + Ccp ± Py ± Moly ± Bn	Py	2.3
WQ13S13	Qtz + K-spar + Bt + Mag + Ccp ± Py ± Moly ± Bn	Py	3.1
WQ13S14	Qtz + K-spar + Bt + Mag + Ccp ± Py ± Moly ± Bn	Moly	5.7
WQ13S15	Qtz + K-spar + Bt + Mag + Ccp ± Py ± Moly ± Bn	Moly	5.0
WQ13S21	Qtz + Moly ± Py ± Ccp	Py	3.5
WQ13S22	Qtz + Moly ± Py ± Ccp	Py	1.6
W-68-1*	Disseminated ore	Moly	5.8
W-24*	Qtz + Moly ± Py ± Ccp	Moly	5.6
M-1*	Qtz + Moly ± Py ± Ccp	Moly	5.5
W9-1*	Qtz + Moly ± Py ± Ccp	Moly	5.7
W18-1*	Qtz + Moly ± Py ± Ccp	Moly	5.6
W20-2*	Qtz + Moly ± Py ± Ccp	Moly	5.5
W-21*	Qtz + Moly ± Py ± Ccp	Moly	5.6
W22-1*	Qtz + Moly ± Py ± Ccp	Moly	6.4
W-46-1*	Qtz + Moly ± Py ± Ccp	Moly	6.6
W-33-1*	Qtz + Moly ± Py ± Ccp	Moly	6.3
W-PD3-1*	Qtz + Moly ± Py ± Ccp	Moly	5.1
W-PD7-2*	Qtz + Moly ± Py ± Ccp	Moly	4.7
WQ13S31	Qtz + Moly ± Py ± Ccp	Moly	5.8
WQ13S32	Qtz + Moly ± Py ± Ccp	Moly	5.8
YDZ-2*	Qtz + Moly ± Py ± Ccp	Moly	6.3
YX-3*	Qtz + Py + Ser + Chl ± Sph	Py	5.6
YX-6*	Qtz + Py + Ser + Chl ± Sph	Py	5.5
W24-1*	Qtz + Py + Ser + Chl ± Sph	Py	5.0
W20-1*	Qtz + Py + Ser + Chl ± Sph	Py	5.6

Note: * samples from He (2012), Han (2009) and Zhu et al. (2011).

4. Analytical results

4.1. Mineral assemblage

The Wenquan deposit displays stockworks veins (Fig. 3A, B, D) typically defined by two or three preferred vein orientations with conjugate or orthogonal relationships, and occur together with sheeted vein arrays (Fig. 3C, D). The scheme of quartz-sulfide vein classification at Wenquan, with distinctive silicate + copper-iron sulfide + oxide assemblages, was determined by previous work and new careful paragenetic study of drill core and hand samples (Fig. 3F). The earliest dark-quartz veinlets with minor copper sulfides (Fig. 3A) are irregular, discontinuous, and segmented. The quartz-chalcopyrite-pyrite veins (Fig. 3B), comprising mineral assemblages of quartz, K-feldspar, biotite, with minor magnetite and pyrite, are generally associated with biotite alteration. The q uartz-chalcopyrite-pyrite-molybdenite veins (Fig. 3C), composed of quartz, K-feldspar, biotite, magnetite and chalcopyrite, with minor pyrite, molybdenite and bornite, are spatially related to potassic alteration in which plagioclase was altered to potassium feldspar. The quartz-molybdenite veins (Fig. 3D), characterized by continuous, planar veins with parallel walls, contain coarse-grained quartz and molybdenite, with minor pyrite and chalcopyrite, which normally occur in cracks or along the margins of molybdenite. Molybdenite grains are predominantly along the contacts between the quartz veins and host granite. The quartz-pyrite-sericite veins (Fig. 3E) represent the final mineralization event at Wenquan. They invariably cut and overprint earlier quartz-sulfide veins, and are also cut by fractures filled with kaolinite and clays. These phyllic veins, with low copper and molybdenum grades, occur as a radial array of continuous, systematically oriented veins (Han, 2009). These late-stage veins comprise abundant euhedral quartz and pyrite, with lesser chalcopyrite, chlorite and sphalerite, and are surrounded by sericitic selvages.

Micropetrography and QEMSCAN analyses indicate that ore minerals are dominated by molybdenite, pyrite, and chalcopyrite, with minor bornite, tetrahedrite, and sphalerite (Fig. 4). Gangue minerals include quartz, calcite, K-feldspar, plagioclase, biotite, sericite, chlorite, epidote, and apatite (Fig. 4). The best developed zones of mineralization are closely associated with potassic- and phyllic-altered porphyries (Fig. 3). The molybdenite aggregates occur normally along the margin of the granites and quartz-stockwork veins (Figs. 3D, 4A, C), and sparsely disseminated in the K-feldspar alteration zone (Fig. 4A, B, C, F). Pyrite, a major constituent of the stockwork ore, is mainly developed in the center of the veins (Fig. 4C, D, F), and is disseminated in the altered granitoids (Fig. 4C). Chalcopyrite, with subordinate pyrite along its margins, and bornite occur as disseminated and late fracture-fillings within the quartz veins (Fig. 4B, E) and intrusions (Fig. 4C). Acces-

Table 3
Fe isotopic compositions of host bulk rocks and pyrite separates at Wenquan.

Sample No.	Sample description	Sample analysed	$\delta^{56}Fe^*$	2se	$\delta^{57}Fe^*$	2se
B02	Biotite-altered porphyry	Whole rock	0.17	0.03	0.30	0.05
B01	Qtz-Ccp-Py vein	Pyrite separate	0.15	0.03	0.21	0.05
C03	Potassic-altered porphyry	Whole rock	0.19	0.03	0.32	0.05
C01	Qtz-Ccp-Py-Moly vein	Pyrite separate	0.17	0.03	0.25	0.05
C02	Qtz-Ccp-Py-Moly vein	Pyrite separate	0.17	0.03	0.27	0.05
D02	Potassic-altered porphyry	Whole rock	0.21	0.03	0.37	0.05
D01	Qtz-Moly vein	Pyrite separate	0.21	0.03	0.31	0.05
E03	Sericitic alteration overprinting early potassic-altered porphyry	Whole rock	0.08	0.03	0.17	0.05
E02	Sericitic-altered porphyry	Whole rock	0.26	0.03	0.42	0.05
E01	Qtz-Py-Ser vein	Pyrite separate	0.32	0.03	0.55	0.05
GSP-2	Granodiorite	Geostandard	0.15	0.03	0.21	0.05
BCR-2	Basalt	Geostandard	0.09	0.03	0.17	0.05

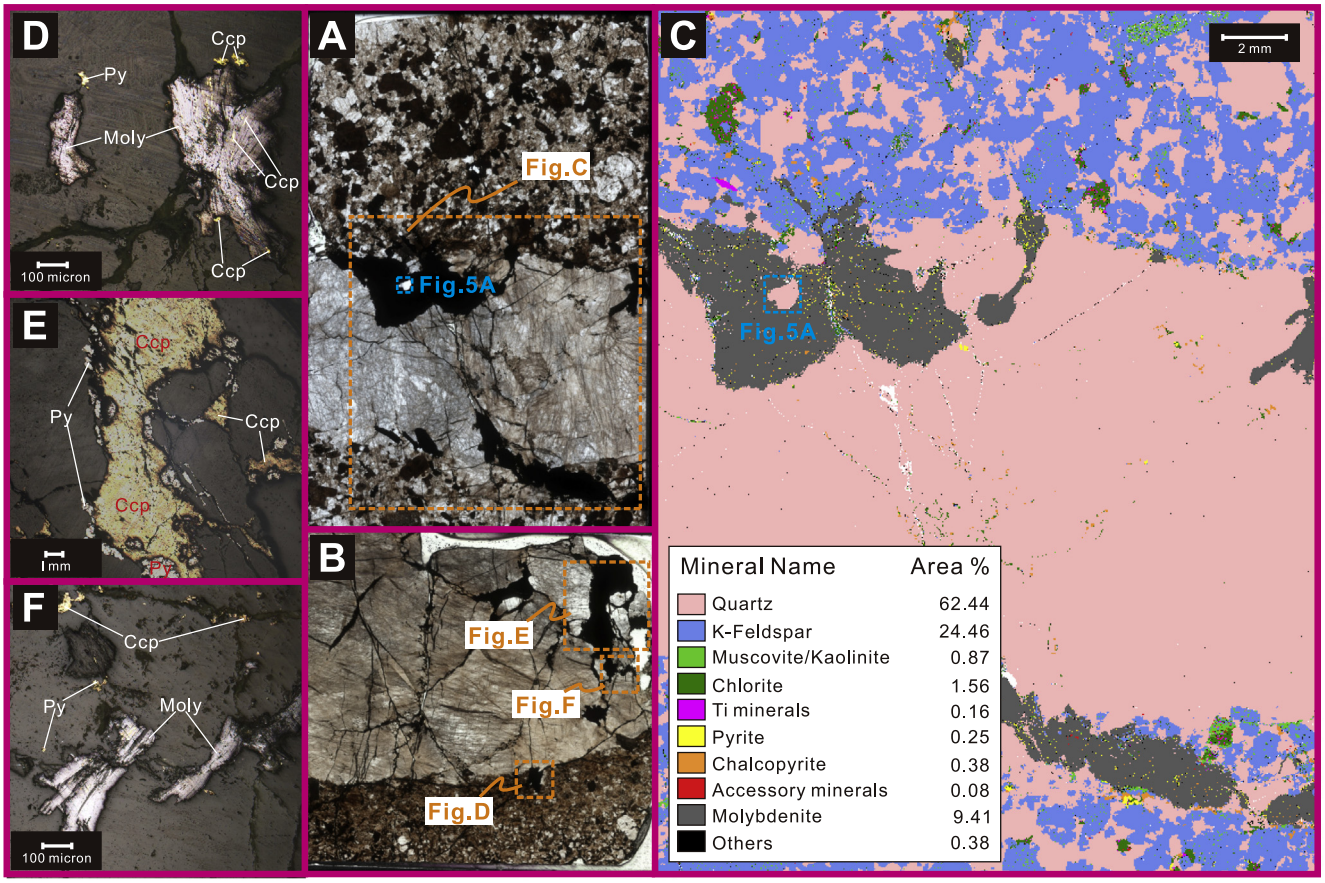

Fig. 4. Scanning thin-section images (A and B), quantitative evaluation of minerals by scanning electron microscopy (QEMSCAN) image (C), and photomicrographs (D, E, F) of quartz-molybdenite veins at Wenquan.

sory phases are Ti-bearing minerals chiefly occurring along margins of vein in alteration halo side. They probably formed as a result of hydrothermal alteration of host porphyries. Gangue minerals including chlorite and muscovite/kaolinite are locally present in secondary alteration processes occur pervasively in the vein selectively, alteration halo and wallrock.

4.2. Fluid inclusion petrography, fluid composition, and temperature/pressure estimates

Dozens of fluid inclusion assemblages, including those dominated by hypersaline inclusions, liquid-rich inclusions, and gas-rich inclusions were observed to be randomly occurring in numerous quartz veins. Only one isolated quartz grain in a quartz-molybdenite vein (W33: Figs 3D, 4C, 5A) was determined to represent the Mo mineralization based on extensive petrographic study, and thus was used for detailed microthermometric investigation. Sample W33 is from a 2-cm-wide planar quartz-molybdenite vein cutting potassically-altered porphyry (Figs 3D, 4A, C). Minor pyrite and chalcopyrite are disseminated in altered porphyry (Fig. 4A, C) and along the cracks or margins of molybdenite aggregates within this quartz vein (Fig. 4B, C, D, F). Pyrite is also rarely present at the margins of chalcopyrite grains (Fig. 4C, E). Three fluid inclusion assemblages (FIAs-1, FIAs-2 and FIAs-3) among numerous fluid inclusions in the isolated quartz within molybdenite aggregates of sample W33 (Fig. 4A, C) were chosen for microthermometry. These three fluid-inclusion assemblages (Fig. 5D, E, F) provide information on the fluid that deposited the coeval molybdenite (Fig. 5A, B, C). Moreover, the FIAs-2 and two molybdenite flakes show a close spatial relationship (Fig. 5C, D). From our perspective, the microthermometric data from these three FIAs provide the most robust PTX information for the molybdenite-bearing fluid at Wenquan.

The isolated quartz (Fig. 4A, C) contains variable numbers of fluid inclusions (Fig. 5A). Three vapor-rich fluid inclusions (Fig. 5C, D, E) within the isolated quartz were selected for microthermometric measurements based on detailed fluid inclusion petrography. The 5–10 μm vapor-rich inclusions are equant to negative-crystal shaped, indicating a relatively high entrapment temperature (cf. Bodnar, 2003), and form clusters or distinct inclusion trails. The FIAs-1 (Fig. 5E) yield homogenization temperatures of 285–290 °C (n = 3). The FIAs-2 (Fig. 5D) closely associated with two molybdenite flakes have homogenization temperatures of 285–290 °C (n = 4). The FIAs-3 (Fig. 5F) have homogenization temperatures of 290–295 °C (n = 4). The ice-melting temperatures of the fluid inclusions in all FIAs are between −4.0 and −3.2 °C, and the presence of clathrate indicates contamination by a non-aqueous phase, likelyCO_2. Therefore the ice melting data only give a maximum salinity, which is <6.5 equiv.wt.% NaCl.

When pressure corrected to 100–150 MPa (4–6 km paleodepth under lithostatic load), which is consistent with the calculated paleodepth of the host porphyries at approximately 5 km (He, 2012). Hydrothermal activity occurred at the same depth of porphyry host emplacement, and the formation temperature is calculated to be ~425 °C by using the calculation proposed by Potter (1977).

4.3. Hydrogen and oxygen isotope data

The temperature used for calculation of the isotopic composition of the hydrothermal K-feldspar from the potassic alteration

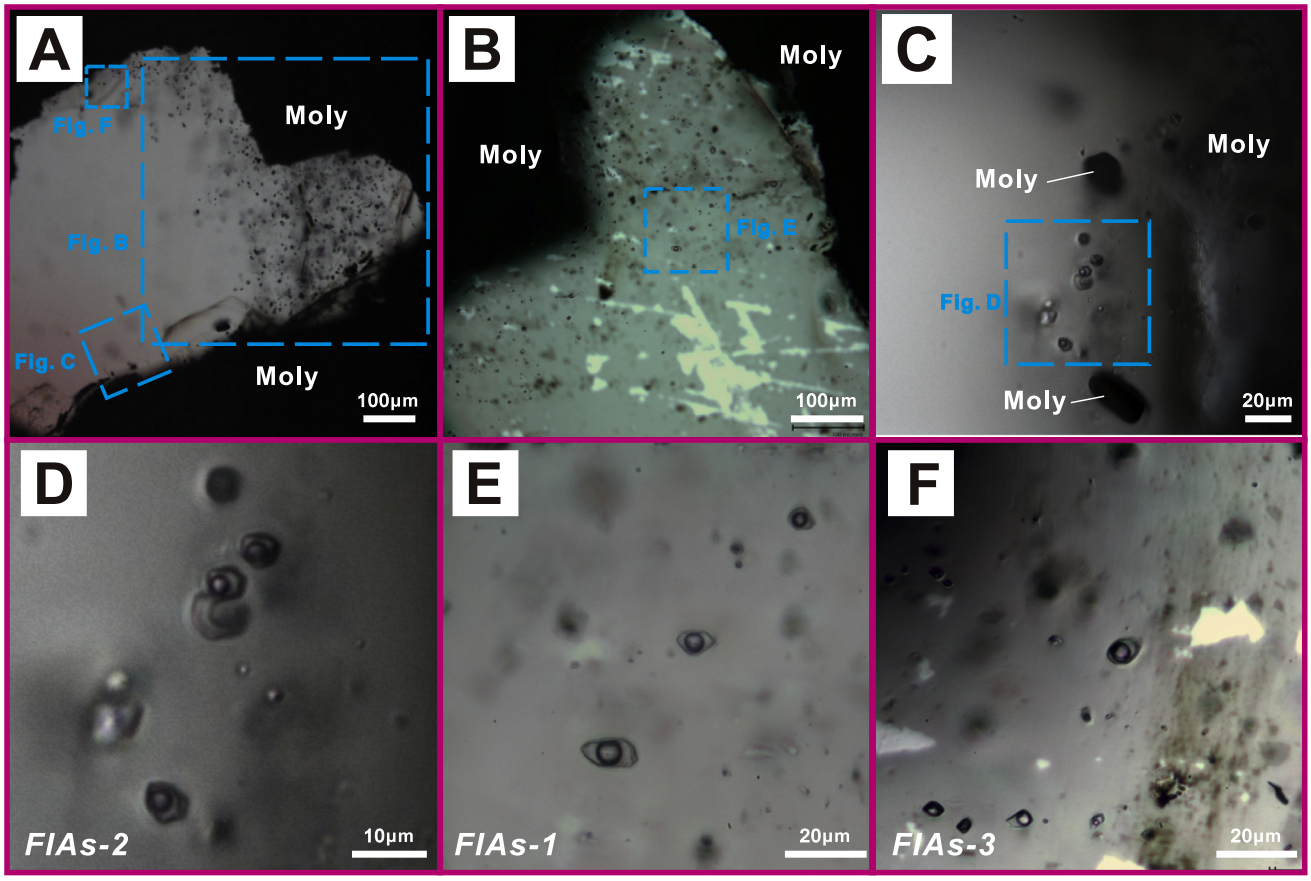

Fig. 5. Photomicrographs of fluid inclusions in the Wenquan porphyry Mo deposit.

(Fig. 3C) is 425 °C, based on the above estimation. The equilibrium temperatures of hydrothermal K-feldspar (550 °C: Rusk et al., 2008) and sericite (300 °C: Han, 2009; Ren, 2009; He, 2012) separates, from a potassic halo surrounding a quartz-molybdenite-pyrite vein (Fig. 3D) and quartz-pyrite-sericite vein (Fig. 3E), were estimated by using the trapping temperature of primary fluid inclusions in quartz coexisting with these different alteration minerals. The measured and calculated oxygen and hydrogen isotopic compositions are listed in Table 1. The analysed hydrothermal K-feldspars have $\delta^{18}O_{mineral}$valuesof + 0.6‰ to +2.8‰, and corresponding calculated $\delta^{18}O_{fluid}$ values of −1.9‰ to +1.9‰. The analysed hydrothermal sericite separates yield δD values from −105 to −98‰, which correspond to calculated δD_{fluid} values from −68 to −60‰. Two hydrothermal sericite separates have $\delta^{18}O_{mineral}$ values of −1.4‰ and +3.6‰, with calculated $\delta^{18}O_{fluid}$ values of −3.7 and +1.4‰. In the $\delta^{18}O_{fluid}$ vs. δD_{fluid} plot (Fig. 6), all samples of early silicates plot in or proximal to the magmatic water field, with later-stage silicates plotting relatively near the meteoric water line (Fig. 6).

4.4. Sulfur isotope data

Sulfur isotope data obtained for nine sulfide minerals from different stages or alteration zones in this study and data from literature are summarized and shown in Fig. 7. One pyrite separate from a quartz-chalcopyrite-pyrite vein crosscutting biotite-altered porphyry yields the lowest $\delta^{34}S$ value of +1.1‰. Two pyrite separates from quartz-chalcopyrite-pyrite-molybdenite veins that crosscut potassically-altered porphyry samples have $\delta^{34}S$ values of +2.3‰ to +3.1‰. Two pyrite separates from quartz-molybdenite-pyrite veins that crosscut potassically-altered porphyry exhibit $\delta^{34}S$ values of +1.6‰ to +3.5‰. Four pyrite separates from the latest quartz-pyrite veins, with sericitic selvages, that crosscut potassically altered porphyries have $\delta^{34}S$ values from +5.0‰ to +5.6‰. Molybdenites from quartz-chalcopyrite-pyrite-molybdenite veins related to potassic alteration have $\delta^{34}S$ values from +5.0‰ to +5.7‰. The quartz-molybdenite veins with minor pyrite and chalcopyrite related to potassic alteration yield $\delta^{34}S$ values for molybdenite of +4.7‰ to +6.6‰.

4.5. Iron isotope data

All samples including geostandards (GSP-2 and BCR-2) analysed in this study define a mass fractionation line in three-isotope space. The correlation between $\delta^{56}Fe$ and $\delta^{57}Fe$ is $\delta^{57}Fe = 1.6248 * \delta^{56}Fe + 0.002$, and $R^2 = 0.9371$ (Fig. 8), indicating no analytical artifacts from unresolved isobaric interferences on Fe isotopes. Considering $\delta^{57}Fe$ is a minor isotope, accurate $^{57}Fe/^{54}Fe$ ratio analyses need relative large ion beams and accordingly more concentrated introducing sample solutions. The Isotope Geochemistry Laboratory at CUGB, which performed the analyses in this study, thus optimizes the conditions for $\delta^{56}Fe$, and therefore data on the $\delta^{56}Fe$ scale is discussed in the manuscript, although theoretically $\delta^{57}Fe = 1.475 * \delta^{56}Fe$.

All analysed bulk samples have $\delta^{56}Fe$ values in a range of 0.08‰ to 0.26‰, with an average of 0.22‰ (Fig. 9), falling within the range of igneous rocks (e.g., Beard et al., 2003; Heimann et al., 2008). The biotite-altered sample (B02) exhibits a $\delta^{56}Fe$ value of 0.17‰, whereas the potassically altered samples (C03 and D02) yield $\delta^{56}Fe$ values of 0.19‰ and 0.21‰. Sample W34 exhibits a

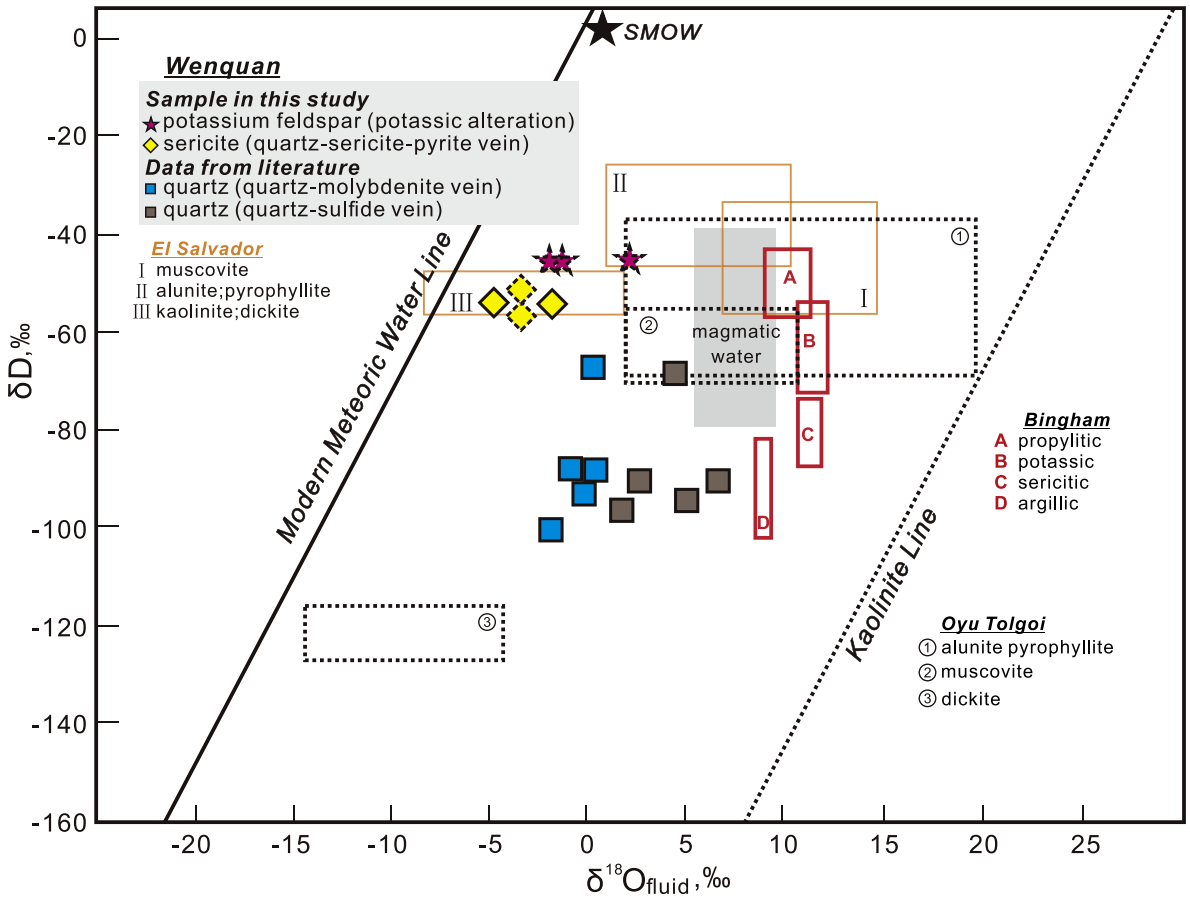

Fig. 6. Plot of calculated δD versus δO for K-feldspar, sericite in this study and quartz from literatures at Wenquan (based map modified after Sheppard et al., 1971), with data of typical porphyry deposits for comparison. Sources of data: magmatic water (Taylor, 1992; Giggenbach, 1992), silicate minerals of different stages including muscovite, alunite, pyrophyllite, kaolinite and dickite at El Salvador (Watanabe and Hedenquist, 2001) and alunite, pyrophyllite, muscovite and dickite at OyuTolgoi (Khashgerel et al., 2008), and evolving alteration stages including propylitic, potassic, phyllicand argillic alteration at Bingham (Bowman et al., 1987). Samples of dashed line symbol indicate that their hydrogen or oxygen isotopic composition were not measured, but assessed from those of associated minerals.

δ^{56}Fe value for potassically altered bulk rock (E03) of 0.08‰, and highest δ^{56}Fe value is for the phyllically altered bulk rock (E02) of 0.26‰.

Five pyrite separates yield δ^{56}Fe values in a range of 0.15‰–0.32‰ (Fig. 9), consistent with the range of igneous rocks (e.g., Beard et al., 2003; Heimann et al., 2008). The δ^{56}Fe value of pyrite (B01) separated from the quartz-chalcopyrite-pyrite vein is 0.15‰, and the pyrites (C01 and C02) separated from the quartz-chalcopyrite-pyrite-molybdenite vein yield δ^{56}Fe values of 0.17‰. The δ^{56}Fe value of pyrite (D01) separated from the quartz-molybdenite-pyrite vein is 0.21‰, whereas the pyrite (E01) separated from the quartz-pyrite-sericite vein exhibits the highest δ^{56}Fe value of 0.32‰.

5. Discussion

5.1. Genetic relationship between Mo mineralization and Wenquan magmatism

Previous geologic studies have established an spatial and temporal relationship between hydrothermal mineral assemblages, abundant stockwork veining, and Triassic porphyries at Wenquan (Han, 2009; Zhu et al., 2009, 2011; Wang, 2011; He, 2012; Qiu et al., 2014, 2015; Xiong et al., 2016). The Mo mineralization at Wenquan is spatially related to the composite granitic pluton (Fig. 3). The main ore minerals (molybdenite, pyrite, and chalcopyrite) are disseminated in the porphyritic phases of the pluton (Figs 4 and 5), and are also ubiquitous in the quartz stockworks, and as infills in joints and cracks in the stockwork veins and their host porphyries (Fig. 5). These mineralization styles are consistent with those of typical porphyry deposits worldwide (Seedorff et al., 2005). Moreover, the granitoids of Wenquan composite display a high degree of crystallization (Han, 2009; Wang, 2011), meaning that that more Mo will be concentrated into the aqueous fluid phase because of its favorable partitioning coefficient.

Previous geochronological data also support a genetic relationship between Mo mineralization and Triassic granite magmatism. Robust U–Pb data on zircons from ore-hosting porphyries and hosted mafic enclaves yield emplacement ages of ca. 225–217 Ma (Cao et al., 2011; Zhu et al., 2011; Xiong et al., 2016). They are identical or slightly older, within analytical error, than Re–Os isochron ages on molybdenite of ca. 219–214 Ma (Song et al., 2008; Xiong et al., 2016). This close spatial and temporal connection between metal precipitation and magma crystallization suggests that the Late Triassic hybrid magma was responsible for generating the Mo mineralization (Cao et al., 2011; Xiong et al., 2016).

Within the porphyritic intrusions, estimated formation depths are 5 km, the early veinlets (Fig. 3A, B) are irregular, discontinuous, and segmented. In contrast, the later quartz-chalcopyrite-pyrite-molybdenite veins (Fig. 3C) and quartz-molybdenite veins (Fig. 3D) tend to be more continuous and planar, some with internal symmetry. This evolution in vein structures is broadly consistent with a transition from >550 °C early-stage vein formation in a ductile crystal mush to formation in a coherent, solidified brittle granite

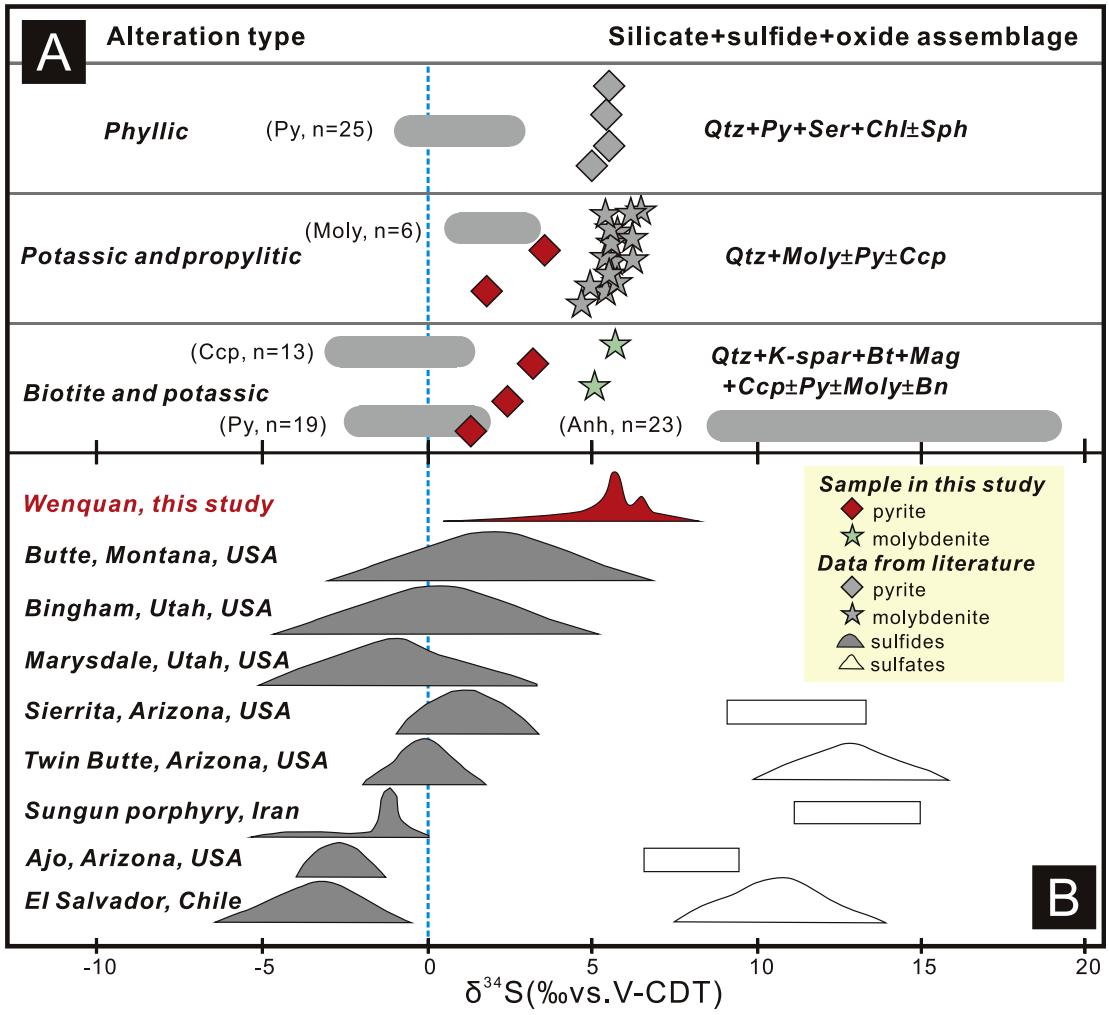

Fig. 7. (A) Sulfur isotopic compositions ($\delta^{34}S‰$) of sulfides separated from different silicate + sulfide + oxide assemblages in the Wenquan porphyry Mo deposit. Data from sulfides and sulfates from the Butte deposit (Field et al., 2005) are plotted for comparison. (B) Histograms of $\delta^{34}S$ values at Wenquan, with data from typical porphyry deposits worldwide for comparison.

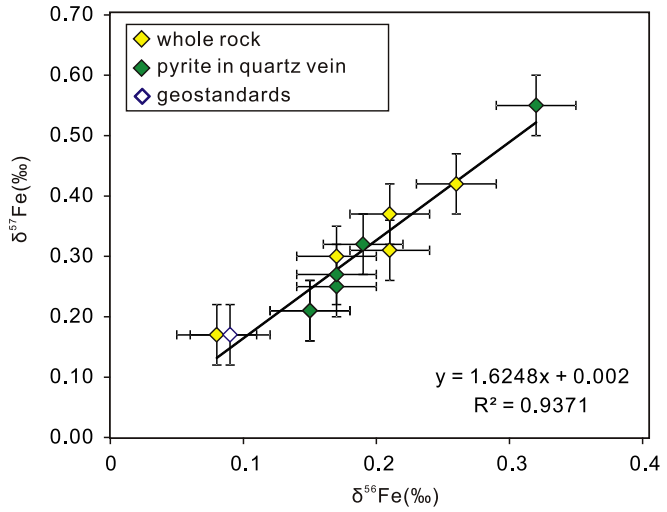

Fig. 8. Plot of measured $\delta^{56}Fe$ versus $\delta^{57}Fe$ values of pyrite separates, whole rocks, and geostandards showing that the Fe isotope data analysed in this study plot on a single mass-fractionation line. Error bars are two standard errors from the internal run statistics.

during potassic alteration. By the time quartz-pyrite-sericite veins (Fig. 3E) form, where euhedral grain textures and open-space fill textures are most common in the phyllic alteration zones, the magmatic-hydrothermal system evolved to lower temperatures (~300 °C) and brittle fractures predominated. The late quartz-pyrite-sericite veins, generally with low Mo and Cu grades, have coarse-grained quartz and pyrite, but no chalcopyrite and molybdenite. They appear to mark the end of the magmatic-hydrothermal system, and probably just complicate the original ore shells by locally redistributing metals to form complex zones of overprinting hydrogen-ion metasomatism.

5.2. Possible fluid sources and evolution: constraints from fluid inclusion and H-O isotope data

Fluid inclusion types in porphyry deposits are well described with respect to pressure and thus paleodepth of emplacement (Bodnar, 2003). Fluids that formed the Wenquan porphyry Mo deposit vary widely in composition, from single-phase and low-salinity aqueous inclusions (this study; Han, 2009; Ren, 2009; He, 2012), through low-salinity vapor inclusions (this study; Han, 2009; Ren, 2009) to dilute liquid to high-salinity brine inclusions (at room temperature; Ren, 2009; He, 2012). The early veins at Wenquan are intimately related to potassic-silicate alteration,

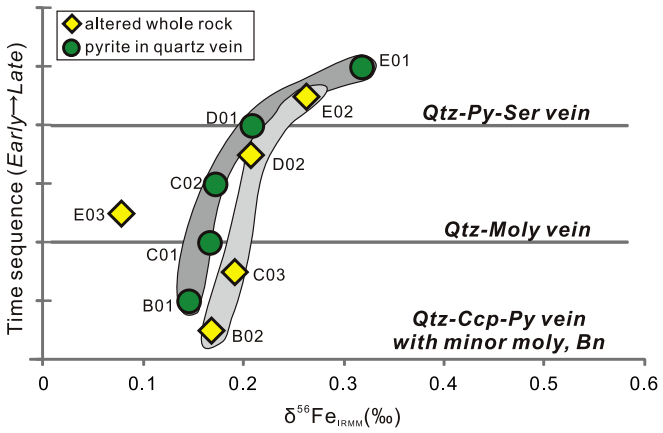

Fig. 9. Iron isotopic compositions (δ^{56}Fe‰) for pyrite separates and bulk samples from the Wenquan Mo deposit.

including biotite and/or K-feldspar, alteration (Fig. 3B, C, D). Fluid inclusion petrography indicates that quartz grains in these veins generally contain a diagnostic primary fluid-inclusion population of coexisting hypersaline brines and low density vapor, for which micro analytical research is critical to understand fluid phase behavior in terms of metallogenesis. During the early potassic-silicate alteration stage, a single-phase fluid unmixes into a hypersaline liquid and a vapor through condensation at a temperature exceeding 550 °C. Hydraulic fracturing under lithostatic conditions causes transient permeability, which could be manifested as permeability waves (Landtwing et al., 2010; Weis et al., 2012; Deng et al., 2015; Wang et al., 2016a), producing irregular, discontinuous, and segmented veins.

The early quartz veins containing Cu-Fe sulphide minerals indicate that extreme metal partitioning occurred in magmatic fluids (Qiu et al., 2015). Such magmatic fluids subsequently underwent immiscibility with the low-salinity and vapor-rich component being significantly metal-enriched compared to coexisting hypersaline liquids (Ren, 2009; He, 2012), similar to that proposed for ore formation in typical porphyry deposits worldwide (Redmond et al., 2004; Pudack et al., 2009; Weis et al., 2012; Liu et al., 2012; Wang et al., 2017). The estimated ore formation temperature of quartz-chalcopyrite veins related to biotite alteration is about 550 °C identical to typical porphyry deposits, and that of quartz-molybdenite veins related to potassic alteration is 425 °C based on calculations in this study. These veins have low-salinity (<6.5 eq. wt.% NaCl), vapor-rich fluid inclusions and locally hypersaline liquid inclusions with an extremely high salinity. As described above, pressure constraints from these inclusions typically indicate shallow conditions (less than 5 km), consistent not only with field observations for subvolcanic emplacement and brittle-stockwork vein systems, but also the observed immiscibility (Muntean and Einaudi, 2001). This pressure includes lithostatic and hydrostatic components because the formation of the Wenquan magmatic-hydrothermal deposits spans the ductile-rittle transition (550–300 °C), where crustal rocks are both resistant to fracturing and fluid circulation under ductile conditions or fracture readily and exhibit enhanced fluid circulation under brittle ones.

Hydrogen and oxygen isotopic signatures show that K-feldspar and sericite from potassic and phyllic assemblages in this study, together with data from ore-bearing quartz veins reported in the literature, plot between the magmatic water field and the meteoric water line (Fig. 6). This suggests that both the early- and late-stage fluids are dominated by magmatic fluids, and the hydrothermal system was subjected to an influx of meteoric water in the late mineralization event. Because the homogenization temperatures of fluid inclusion assemblages used for calculation of the fluid isotope values generally represent the minimum trapping temperature of the ore-forming fluids, presented $\delta^{18}O_{fluid}$ values could be erroneously low. Our refined H-O isotopic compositions suggest that ore fluid compositions varied through time. Early potassic alteration is characterized by fluid compositions similar to magmatic water ($\delta^{18}O_{fluid}$ from 5 to 9‰, and δD from −20 to −80‰: Giggenbach, 1992; Taylor, 1992; John et al., 2010), as observed in some typical porphyry deposits around the world, such as from the early alteration phases at El Salvador (Watanabe and Hedenquist, 2001), Bingham (Bowman et al., 1987), and OyuTolgoi (Khashgerel et al., 2008). In contrast, later stage sericite from phyllic alteration is characterized by $\delta^{18}O_{fluid}$ values that are nearer to the meteoric water line or lower $\delta^{18}O_{fluid}$ isotopic values (Fig. 6), consistent with those at Bingham (Bowman et al., 1987) and OyuTolgoi (Khashgerel et al., 2008), reflecting the input of meteoric water during phyllic alteration under a hydrostatic load.

The δD fluid values related to different ore and alteration stages within the Wenquan system also vary over a large range. This may indicate that the δD values are controlled by magma degassing, in addition to mixing of early magmatic and later meteoric waters, similar to what is observed at the Bingham (Bowman et al., 1987) and OyuTolgoi (Khashgerel et al., 2008) porphyry deposits. This is because the later open-system degassing, where exsolved volatiles separate from magma, generally results in more variable δD values than an earlier closed-system, where exsolved volatiles and magma co-exist.

In summary, based on a detailed study of the paragenesis of alteration and mineralization, and fluid inclusion and H-O data at Wenquan, it is proposed that both the Triassic intrusive rocks and fluids responsible for mineralization were derived from a deeper magma chamber with a paleodepth of 5 km under a lithostatic load (Fig. 10A). However, external fluids were likely involved during the late stage of ore formation spanning the ductile-brittle transition under a hydrostatic load (Fig. 10B).

5.3. Sulfur and iron isotope implications for metal sources

The average $\delta^{34}S$ values of sulfide minerals are considered to represent the $\delta^{34}S$ composition of hydrothermal fluids because $\delta^{34}S_{sulfide} \approx \delta^{34}S_{H2S} \approx \delta^{34}S_{fluid}$ in hydrothermal systems, where H_2S is the dominant sulfur species in the fluids or the fluid redox state is below the SO_2/H_2S boundary (Kelly and Rye, 1979; Rollinson, 1993). As discussed above, quartz stockwork veins at Wenquan have pyrite and molybdenite as the main sulfides, and lack oxide phases and sulfate minerals, suggesting that H_2S was the dominant sulfur species, and therefore the average $\delta^{34}S$ values of pyrite and molybdenite represent the $\delta^{34}S$ composition of the hydrothermal fluids. Sulfur isotopic signatures of all analysed molybdenite and pyrite separates yield $\delta^{34}S$ values ranging from 1.1‰ to 6.6‰ (Fig. 7A), with an average of 4.5‰. These relatively homogeneous $\delta^{34}S$ values of the Wenquan deposit are consistent with those of the fluids in equilibrium with porphyry magmas ($\delta^{34}S$ = 0.0‰: Ohmoto, 1972), suggesting a magmatic origin for sulfur and metal sources. The $\delta^{13}C_{PDB}$ values (−8.3‰ to −7.9‰: Wang et al., 2012) of calcite separated from post-mineralization calcite-quartz veins are consistent with those of typical magmatic sources (−8‰ to −4‰: Ohmoto, 1972; Pirajno, 2016), indicating the carbon at Wenquan had a dominant magmatic source.

A declining/increasing trend of $\delta^{34}S$ values is documented from many different metal-bearing porphyry systems (e.g., Wenquan, Butte, Bingham, Marysdale, Sierrita, Twin Butte, Sungun, Ajo and El Salvador). When compared to these porphyry deposits, the Wenquan deposit has relatively heavy sulfur, similar to Butte and Bingham (Fig. 7B). Ohmoto and Rye (1979) pointed out that $\delta^{34}S$ values are very sensitive to the oxidation state of the fluid, which is largely determined by H_2S/SO_4^{2-}, and temperature. As mentioned

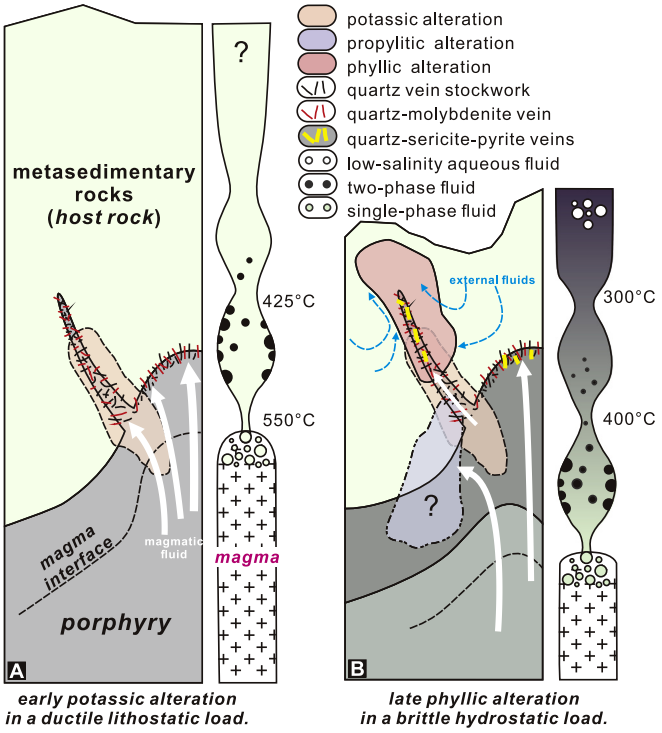

Fig. 10. Schematic model for formation of the Wenquan porphyry Mo deposit, illustrating the inferred fluid evolution paths from the deep lithostatic to the shallow hydrostatic environment (Modified after Seedorff et al., 2008; Pudack et al., 2009; John et al., 2010).

above, temperatures of the early potassic alteration stage are higher than those of the late phyllic alteration stage in the Wenquan magmatic-hydrothermal system (Klemm et al., 2008; Audetat et al., 2008, 2011). Therefore, the heavy $\delta^{34}S$ values for early sulfides could be interpreted to reflect late incorporation of isotopically heavy evaporate sulfate into the porphyry magma (Field et al., 2005; Rye, 2005; John et al., 2010; Liu et al., 2011; Zhang et al., 2014; Yang et al., 2016; Wang et al., 2016b) from underlying Devonian sedimentary rocks. The Pb isotopes of bulk samples and K-feldspar from Wenquan porphyry samples plot close to the orogenic Pb evolution line, and between the upper crust and mantle Pb evolution lines. This indicates that the granitic magmas were sourced from the middle-lower crust with lesser involvement of mantle-derived materials. Moreover, the ore-forming materials could be incorporated into the hydrothermal fluid during differentiation of the Triassic magmatic system with only a minor contribution of sedimentary country rock (Wang, 2011; Zhu et al., 2011; He, 2012).

Anbar and Rouxel (2007) reviewed iron isotopic composition reservoirs, including$\delta^{56}Fe$ values of igneous rocks (0.1‰), deep sea clays (−0.1‰), altered oceanic crust (−1.5–1.5‰), aerosols (0.1‰), and rivers (−1 to 0‰); the altered oceanic crust yields the most variable $\delta^{56}Fe$ compositions probably due to its complex formation. The $\delta^{56}Fe$ values of the altered intrusive rocks (0.08–0.26‰) and pyrite separates (0.15–0.32‰) from Wenquan are higher and more variable that that of unaltered igneous rocks. This relatively wide range of $\delta^{56}Fe$ values may be attributed to variable degrees of fluid:rock interaction. The $\delta^{56}Fe$ values of pyrite separates are positively correlated to those of bulk samples (Fig. 9), indicating their possible relationship on metal sources. Moreover, the $\delta^{56}Fe$ values for pyrite are generally slightly lower than those of their host granitoid samples, suggesting that iron in pyrite is sourced, or at least partially sourced, from altered porphyries. The $\delta^{56}Fe$ values of both bulk samples and pyrite grains related to early biotite, potassic, and later phyllic alteration show a declining trend with time, and are enriched in heavy Fe, which indicates $\delta^{56}Fe$ in the hydrothermal system at Wenquan became lighter as it transitioned from an early lithostatic to late hydrostatic regime.

In conclusion, it is suggested that early potassic-silicate alteration assemblages formed under lithostatic loads at temperatures ranging from 550 to 425 °C, with high water-rock interaction and wallrock buffering. This resulted in progressive alteration zonation from the center outward in the Wenquan magmatic-hydrothermal system (Fig. 10A). Transitions to phyllic alteration correlate with a progression from lithostatic to hydrostatic load at 300 °C, possibly due to the ingress of meteoric water. Such a process marks the end of porphyry ore formation. Sulfur and metals in the Wenquan Mo deposit mainly originated from a magmatic-hydrothermal fluid associated with crystallization of granitic magmas. They were possibly incorporated by contamination from the underlying Devonian sedimentary rocks during the late stage (Fig. 10B).

6. Conclusions

Geologic, petrographic, and fluid-chemical-isotopic evidence indicate that the formation of the Wenquan porphyry Mo deposit involves an interplay between magmatic metal sources and hydrothermal fluid systems in spatially, temporally, and genetically related Triassic porphyries. An early, high-temperature hypersaline fluid of magmatic origin resulted in potassic alteration under a lithostatic load, whereas phyllic alteration under a hydrostatic load likely formed from lower-temperature and less-saline non-magmatic meteoric or formation water. The bulk of the metals were precipitated from an expanding vapor-rich fluid, coexisting with a hypersaline fluid, both of which were derived from cooling and expansion of a single-phase fluid exsolved during magma crystallization. The timing of deposit formation was during Late Triassic collision between the South China and North China Blocks. The sulfur and metals were likely derived from a hybrid magma, and they were originated from lower crust and mantle due to deep magma mixing, with possible incorporation from the underlying Devonian sedimentary rocks at a higher crustal level.

Acknowledgments

David Groves, Richard Goldfarb and Jun Deng are appreciated for their constructive editing. Ryan Taylor, Wang-Zhen Han, Yao-Hui Song and Kai-Rui Song are acknowledged for the assistance in the field. Special thanks go to James Reynolds from FLUID INC. and Mitchell Bennett from USGS for many critical discussions on fluid inclusions, and Craig Johnson from USGS and Yong-Sheng He from CUGB for stable isotope interpretation. I also owe a debt of gratitude to Thomas Monecke from Colorado School of Mines and Heather Lowers from USGS for discussion and assistance on the CL imaging and electron microprobe. Constructive and critical comments from Franco Pirajno, Karen Kelley at USGS and two anonymous reviewers greatly improving the quality of this paper are highly appreciated. This research was financially supported by the National Basic Research Program (2015CB452605), 111 Project (B07011) and Geological investigation work project of China Geological Survey (1212011121090). The senior author was the recipient of a China Postdoctoral Science Foundation (2016M591221), Key Laboratory of Western Mineral Resources and Geological Engineering of Ministry of Education (310826171109), Society of Economic Geologists Foundation, and China Scholarship Council grants, which are gratefully acknowledged. Any use of trade, product, or firm names is for descriptive purposes only and does not imply endorsement by the U.S. Government.

References

Anbar, A.D., Rouxel, O., 2007. Metal stable isotopes in paleoceanography. Ann. Rev. Earth Planet. Sci. 35, 717–746.

Audetat, A., Pettke, T., Heinrich, C.A., Bodnar, R.J., 2008. Special paper: the composition of magmatic-hydrothermal fluids in barren and mineralized intrusions. Econ. Geol. 103 (5), 877–908.

Audetat, A., Dolejs, D., Lowenstern, J.B., 2011. Molybdenite saturation in silicic magmas: occurrence and petrological implications. J. Petrol. 52 (5), 891–904.

Beard, B.L., Johnson, C.M., Skulan, J.L., Nealson, K.H., Cox, L., Sun, H., 2003. Application of Fe isotopes to tracing the geochemical and biological cycling of Fe. Chem. Geol. 195, 87–117.

Bian, Q.T., Li, D.H., Pospelov, I., Yin, L.M., Li, H.S., Zhao, D.S., Chang, C.F., Luo, X.Q., Gao, S.L., Astrakhantsev, O., Chamov, N., 2004. Age, geochemistry and tectonic setting of Buqingshan ophiolites, North Qinghai-Tibet Plateau, China. J. Asian Earth Sci. 23, 577–596.

Bodnar, R.J., 2003. Reequilibration of fluid inclusions. In: Samson, I., Anderson, A., Marshall, D. (Eds.), Fluid inclusion-analysis and interpretation, Geological Association of Canada Short Course Series, vol. 32, pp. 213–231.

Bowman, J.R., Parry, W.T., Kropp, W.P., Kruer, S.A., 1987. Chemical and isotopic evolution of hydrothermal solutions at Bingham, Utah. Econ. Geol. 82, 395–428.

Calagari, A.A., 2003. Stable isotope (S, O, H and C) studies of the phyllic and potassic–phyllic alteration zones of the porphyry copper deposit at Sungun, East Azarbaidjan, Iran. J. Asian Earth Sci. 21, 767–780.

Cao, X.F., Lü, X.B., Yao, S.Z., Mei, W., Zou, X.Y., Chen, C., Liu, S.T., Zhang, P., Su, Y.Y., Zhang, B., 2011. LA-ICP-MS U-Pb zircon geochronology, geochemistry and kinetics of the Wenquan ore-bearing granites from West Qinling, China. Ore Geol. Rev. 43, 120–131.

Chen, Y.J., Santosh, M., 2014. Triassic tectonics and mineral systems in the Qinling Orogen, China. Geol. J. 49 (4–5), 338–358.

Chen, Y.J., Zhang, C., Wang, P., Pirajno, F., Li, N., 2017. The Mo deposits of Northeast China: a powerful indicator of tectonic settings and associated evolutionary trends. Ore Geol. Rev. 81, 602–640.

Clayton, R., Mayeda, T.K., 1963. The use of bromine pentafluoride in the extraction of oxygen from oxides and silicates for isotopic analysis. Geochim. Cosmochim. Acta 27, 43–52.

Coleman, M.L., Shepherd, T.J., Durham, J.J., et al., 1982. Reduction of water with zinc for hydrogen isotope analysis. Anal. Chem. 54, 993–995.

Dauphas, N., van Zuilen, M., Wadhwa, M., Davis, A.M., Marty, B., Janney, P.E., 2004. Clues from Fe isotope variations on the origin of Early Archean BIFs from Greenland. Science 306, 2077–2080.

Deng, J., Wang, Q.F., 2016. Gold mineralization in China: Metallogenic provinces, deposit types and tectonic framework. Gondwana Res. 36, 219–274.

Deng, J., Ge, L.S., Yang, L.Q., 2013. Tectonic dynamic system and compound orogeny: additionally discussing the temporal-spatial evolution of Sanjiang orogeny, Southwest China. Acta Petrol. Sin. 29, 1099–1114 (in Chinese with English abstract).

Deng, J., Wang, Q.F., Li, G.J., Santosh, M., 2014a. Cenozoic tectono-magmatic and metallogenic processes in the Sanjiang region, southwestern China. Earth-Sci. Rev. 138 (11), 268–299.

Deng, J., Wang, Q.F., Li, G.J., Li, C.S., Wang, C.M., 2014b. Tethys tectonic evolution and its bearing on the distribution of important mineral deposits in the Sanjiang region, SW China. Gondwana Res. 26, 419–437.

Deng, J., Wang, Q.F., Li, G.J., Hou, Z.Q., Jiang, C.Z., Danyushevsky, L., 2015. Geology and genesis of the giant Beiya porphyry-skarn gold deposit, northwestern Yangtze Block, China. Ore Geol. Rev. 70, 457–485.

Dong, Y.P., Santosh, M., 2016. Tectonic architecture and multiple orogeny of the Qinling Orogenic Belt, Central China. Gondwana Res. 29 (1), 1–40.

Dong, Y.P., Yang, Z., Liu, X.M., Sun, S.S., Li, W., Cheng, B., Zhang, F.F., Zhang, X.N., He, D.F., Zhang, G.W., 2016. Mesozoic intracontinental orogeny in the Qinling Mountains, central China. Gondwana Res. 30, 144–158.

Field, C.W., Zhang, L., Dilles, J.H., Rye, R.O., Reed, M.H., 2005. Sulfur and oxygen isotopic record in sulfate and sulfide minerals of early, deep, pre-Main Stage porphyry Cu–Mo and late Main Stage base-metal mineral deposits, Butte district, Montana. Chem. Geol. 215, 61–93.

Giesemann, A., Jager, H.J., Norman, A.L., et al., 1994. Online sulfur-isotope determination using an elemental analyzer coupled to a mass-spectrometer. Anal. Chem. 66, 2816–2819.

Giggenbach, W.F., 1992. Isotopic shifts in waters from geothermal and volcanic systems along convergent plate boundaries and their origin. Earth Planet. Sci. Lett. 113, 495–510.

Goldfarb, R.J., Groves, D.I., 2015. Orogenic gold: common or evolving fluid and metal sources through time. Lithos 233, 2–26.

Goldstein, R.H., Reynolds, T.J., 1994. Systematics of fluid inclusions in diagenetic minerals. Soc. Econ. Mineralogists Paleontologists short course 31, 1–199.

Gansu Bureau of Geology and Mineral Exploration (GSBGME), 1979. Magmatic and hydrothermal copper deposit in the Western Qinling. Northwestern Geol. 2, 32–41 (in Chinese).

Han, H.T., 2009. Geochemical Characteristics and Metallogenic Prediction of the Wenquan Molybdenum Deposit in the Western Qinling (Ph.D. thesis). Central South University, Changsha, pp. 1-116 (in Chinese with English abstract).

He, M.C., 2012. Mo-W-Cu Metallogenic System Related to Mesozoic Granite in West Qinling Region (Ph.D. thesis). China University of Geosciences, Wuhan, pp. 1-129 (in Chinese with English abstract).

He, Y.S., Ke, S., Teng, F.Z., Wang, T.T., Wu, H.J., Lu, Y.H., Li, S.G., 2015. High precision iron isotope analysis of geological reference materials by High Resolution MC-ICP-MS. Geostand. Geoanal. Res. 39, 341–356.

Heimann, A., Beard, B.L., Johnson, C.M., 2008. The role of volatile exsolution and subsolidus fluid/rock interactions in producing high $^{56}Fe/^{54}Fe$ rations in siliceous igneous rocks. Geochim. Cosmochim. Acta 72, 4379–4396.

John, D.A., Ayuso, R.A., Barton, M.D., Blakely, R.J., Bodnar, R.J., Dilles, J.H., Gray, Floyd. Graybeal, F.T., Mars, J.C., McPhee, D.K., Seal, R.R., Taylor, R.D., Vikre, P.G., 2010. Porphyry copper deposit model, chap. B of Mineral deposit models for resource assessment. U.S. Geological Survey Scientific Investigations Report 2010-5070-B. 169 pp.

Kelly, W.C., Rye, R.O., 1979. Geological, fluid inclusion and stable isotope studies of the tin–tungsten deposits of Panasqueira, Portugal. Econ. Geol. 74, 1721–1822.

Khashgerel, B.E., Kavalieris, I., Hayashi, K.I., 2008. Mineralogy, textures, and whole-rock geochemistry of advanced argillic alteration—Hugo Dummett porphyry copper-Au deposit, Oyu Tolgoi mineral district, Mongolia. Miner. Deposita 43, 913–932.

Klemm, L.M., Pettke, T., Heinrich, C.A., 2008. Fluid and source magma evolution of the Questa porphyry Mo deposit, New Mexico, USA. Miner. Deposita 43 (5), 533–552.

Landtwing, M.R., Furrer, C., Redmond, P.B., Pettke, T., Guillong, M., Heinrich, C.A., 2010. The Bingham Canyon porphyry Cu-Mo-Au deposit. III. Zoned copper- gold ore deposition by magmatic vapor expansion. Econ. Geol. 105, 91–118.

Li, N., Pirajno, F., 2017. Early mesozoic Mo mineralization in the qinling orogen: an overview. Ore Geol. Rev. 81, 431–450.

Li, N., Chen, Y.J., Pirajno, F., Ni, Z.Y., 2013. Timing of the Yuchiling giant porphyry Mo system, and implications for ore genesis. Miner. Deposita 48, 505–524.

Li, N., Deng, J., Yang, L.Q., Goldfarb, R.J., Zhang, C., March, E., Lei, S.B., Koenig, A., Lowers, H., 2014. Paragenesis and geochemistry of ore minerals in the epizonal gold deposits of the Yangshan gold belt, West Qinling, China. Miner. Deposita 49, 427–449.

Liu, Y., Deng, J., Zhang, G.B., Shi, G.H., Yang, L.Q., Wang, Q.F., 2010. $^{40}Ar/^{39}Ar$ Dating of Xuebaoding granite in the Songpan-Ganze Orogenic belt, Southwest China, and its Geological Significance. Acta Geol. Sin. (English Edition) 84 (2), 345–357.

Liu, Y., Deng, J., Shi, G.H., Sun, X., Yang, L.Q., 2011. Geochemistry and petrogenesis of placer nephrite in Hetian, Xinjiang, northwest China. Ore Geol. Rev. 41, 122–132.

Liu, Y., Deng, J., Shi, G.H., Sun, X., Yang, L.Q., 2012. Genesis of the Xuebaoding W-Sn-Be crystal deposits in Southwest China: evidence from fluid inclusions, stable isotopes and ore elements. Resour. Geol. 62 (2), 159–173.

Liu, Y., Zhang, R.Q., Zhang, Z.Y., Shi, G.H., Zhang, Q.C., Abuduwayiti, M., Liu, J.H., 2015. Mineral inclusions and SHRIMP U-Pb dating of zircons from the Alamas nephrite and granodiorite: implications for the genesis of a magnesian skarn deposit. Lithos 212–215, 128–144.

Luo, B.J., Zhang, H.F., Lü, X.B., 2012. U-Pb zircon dating, geochemical and Sr-Nd-Hf isotopic compositions of Early Indosinian intrusive rocks in West Qinling, central China: petrogenesis and tectonic implications. Contrib. Miner. Petrol. 164, 551–569.

Mao, J.W., Xie, G.Q., Bierlein, F., Qu, W.J., Du, A.D., Ye, H.S., Pirajno, F., Li, H.M., Guo, B. J., Li, Y.F., Yang, Z.Q., 2008. Tectonic implications from Re–Os dating of Mesozoic molybdenum deposits in the East Qinling-Dabie orogenic belt. Geochim. Cosmochim. Acta 72, 4607–4626.

Marumo, K., Nagasawa, K., Kuroda, Y., 1980. Mineralogy and hydrogen isotope geochemistry of clay minerals in the Ohnuma geothermal area, Northeastern Japan. Earth Planet. Sci. Lett. 47, 255–262.

Meng, Q.R., Zhang, G.W., 2000. Geologic framework and tectonic evolution of the Qinling orogen, central China. Tectonophysics 323, 183–196.

Muntean, J.L., Einaudi, M.T., 2001. Porphyry-epithermal transition: maricunga belt, northern Chile. Econ. Geol. 96, 743–772.

Ohmoto, H., 1972. Systematics of sulfur and carbon isotopes in hydrothermal ore deposits. Econ. Geol. 67, 551–579.

Ohmoto, H., Rye, R.O., 1979. Isotopes of sulfur and carbon. In: Barnes, H.L. (Ed.), Geochemistry of Hydrothermal Ore Deposits. second ed. John Wiley and Sons, New York, pp. 509–567.

Pirajno, F., 2016. A classification of mineral systems, overviews of plate tectonic margins and examples of ore deposits associated with convergent margins. Gondwana Res. 33, 44–62.

Pirajno, F., Zhou, T.F., 2015. Intracontinental porphyry and porphyry-skarn mineral systems in Eastern China: scrutiny of a special Case "Made-in-China". Econ. Geol. 110, 603–629.

Potter, R.W., 1977. Pressure correction for fluid inclusion homogenization temperature based on the volumetre properities of the system $NaCl-H_2O$. J. Res. U.S. Geol. Surv. 5, 603–607.

Pudack, C., Halter, W.E., Heinrich, C.A., Pettke, T., 2009. Evolution of magmatic vapor to gold-rich epithermal liquid: the porphyry to epithermal transition at Nevados de Famatina, northwest Argentina. Econ. Geol. 104, 449–477.

Qiu, K.F., Deng, J., 2016. Petrogenesis of granitoids in the Dewulu skarn copper deposit: Implications for the evolution of the Paleotethys ocean and mineralization in Western Qinling, China. Ore Geol. Rev. http://dx.doi.org/10.1016/j.oregeorev.2016.09.027.

Qiu, K.F., Li, N., Taylor, R.D., Song, Y.H., Song, K.R., Han, W.Z., Zhang, D.X., 2014. Timing and duration of metallogeny of the Wenquan deposit in the West Qinling, and its constraint on a proposed classification for porphyry molybdenum deposits. Acta Petrol. Sin. 30, 2631–2643 (in Chinese with English abstract).

Qiu, K.F., Song, K.R., Song, Y.H., 2015. Magmatic-hydrothermal fluid evolution of the Wenquan porphyry molybdenum deposit in the north margin of the Western Qinling, China. Acta Petrol. Sin. 31 (11), 3391–3404 (in Chinese with English abstract).
Qiu, K.F., Taylor, R.D., Song, Y.H., Yu, H.C., Song, K.R., Li, N., 2016. Geologic and geochemical insights into the formation of the Taiyangshan porphyry copper-molybdenum deposit, Western Qinling Orogenic Belt, China. Gondwana Res. 35, 40–58.
Ratschbacher, L., Hacker, B.R., Calvert, A., Webb, L.E., Grimmer, J.C., McWilliams, M. O., Ireland, T., Dong, S.W., Hu, J.M., 2003. Tectonics of the Qinling (central China): tectonostratigraphy, geochronology, and deformation history. Tectonophysics 366, 1–53.
Redmond, P.B., Einaudi, M.T., Inan, E.E., Landtwing, M.R., Heinrich, C.A., 2004. Copper deposition by fluid cooling in intrusion-centered systems: new insights from the Bingham porphyry ore deposit, Utah. Geology 32, 217–220.
Ren, X.H., 2009. Geological characteristics and genesis of molybdenum deposits in Wushan County of Gansu. Gansu Metall. 31 (6), 58–61 (in Chinese with English abstract).
Rollinson, H.R., 1993. Using Geochemical Data: Evaluation, Presentation, Interpretation. Longman Scientific and Technical Press, pp. 306–308.
Rusk, B.G., Reed, M.H., Dilles, J.H., Kent, A.J.R., 2006. Intensity of quartz cathodoluminescence and trace-element content in quartz from the porphyry copper deposit at Butte, Montana. Am. Mineral. 91, 1300–1312.
Rusk, B.G., Lowers, H.A., Reed, M.H., 2008. Trace elements in hydrothermal quartz: relationships to cathodoluminescent textures and insights into vein formation. Geology 36, 547–550.
Rye, R.O., 2005. A review of the stable isotope geochemistry of sulfate minerals in selected igneous environment and related hydrothermal systems. Chem. Geol. 215, 5–36.
Seedorff, E., Dilles, J.H., Proffett, J.M., Einaudi, M.T., Zurcher, L., Stavast, W.J., Johnson, D.A., Barton, M.D., 2005. Porphyry deposits: characteristics and origin of hypogene features. Econ. Geol. 100, 251–298.
Seedorff, Eric., Barton, M.D., Stavast, W.J.A., Maher, D.J., 2008. Root zones of porphyry systems—extending the porphyry model to depth. Econ. Geol. 103, 939–956.
Sheppard, S.M.F., Nielsen, R.L., Taylor, H.P., 1971. Hydrogen and oxygen isotope ratios in minerals from porphyry copper deposits. Econ. Geol. 66, 515–542.
Song, S.G., Ding, Z.J., Yao, S.Z., Zhou, Z.G., Zhang, S.X., Du, A.D., 2008. Re–Os isotopic dating of molybdenite and its implication for molybdenum mineralization of Wenquan Porphyry, Wushan, Gansu Province. Northwestern Geol. 41, 67–73 (in Chinese).
Tang, L., Santosh, M., Dong, Y.P., 2015. Tectonic evolution of a complex orogenic system: evidence from the northern Qinling belt, central China. J. Asian Earth Sci. 113, 544–559.
Tang, L., Santosh, M., Dong, Y.P., Tsunogae, T., Zhang, S.T., Cao, H.W., 2016. Early Paleozoic tectonic evolution of the North Qinling orogenic belt: evidence from geochemistry, phase equilibrium modeling and geochronology of metamorphosed mafic rocks from the Songshugou ophiolite. Gondwana Res. 30, 48–64.
Taylor, B.E., 1992. Degassing of H_2O from rhyolitic magma during eruption and shallow intrusion, and the isotopic composition of magmatic water in hydrothermal systems. Geol. Surv. Jpn. Rep. 279, 190–194.
Wang, F., 2011. The Geological and Geochemical Characteristics of the Wenquan Molybdenum Deposit in the West Qinling, and Its Metallogenetic Geodynamic Setting (Master thesis). Northwest University, Xi'an, pp. 1-96 (in Chinese with English abstract).
Wang, F., Zhu, L.M., Guo, B., Yang, T., Luo, Z.Z., 2012. Geological and geochemical characteristics of the Wenquan molybdenum deposit and ore-forming process in the western Qinling. Geol. Explor. 48, 713–727 (in Chinese with English abstract).
Wang, X.X., Wang, T., Zhang, C.L., 2013. Neoproterozoic, Paleozoic, and Mesozoic granitoid magmatism in the Qinling Orogen, China: constraints on orogenic process. J. Asian Earth Sci. 72, 129–151.
Wang, Q.F., Deng, J., Li, C.S., Li, G.J., Yu, L., Qiao, L., 2014. The boundary between the Simao and Yangtze blocks and their locations in Gondwana and Rodinia: constraints from detrital and inherited zircons. Gondwana Res. 26, 438–448.
Wang, C.M., Bagas, L., Lu, Y.J., Santosh, M., Du, B., McCuaig, T.C., 2016a. Terrane boundary and spatio-temporal distribution of ore deposits in the Sanjiang Tethyan Orogen: insights from zircon Hf-isotopic mapping. Earth Sci. Rev. 156, 39–65.
Wang, Y.H., Xue, C.J., Liu, J.J., Zhang, F.F., 2016b. Geological, geochronological, geochemical, and Sr–Nd–O–Hf isotopic constraints on origins of intrusions associated with the Baishan porphyry Mo deposit in eastern Tianshan, NW China. Miner. Deposita 51, 953–969.
Wang, Y.H., Zhang, F.F., Li, B.C., 2017. Genesis of the Yandong porphyry Cu deposit in eastern Tianshan, NW China: Evidence from geology, fluid inclusions and isotope systematics. Ore Geol. Rev. 86, 280–296.
Watanabe, Yasushi, Hedenquist, J.W., 2001. Mineralogic and stable isotope zonation at the surface over El Salvador porphyry copper deposit, Chile. Econ. Geol. 96, 1775–1797.
Weis, P., Driesner, T., Heinrich, C.A., 2012. Porphyry-copper ore shells form at stable pressure temperature fronts within dynamic fluid plumes. Science 338, 1613–1616.
Whitney, D.L., Evans, B.W., 2010. Abbreviations for names of rock-forming minerals. Am. Mineral. 95, 185–187.
Xiang, D.P., Tao, B.K., Wu, Y.J., Zou, E.M., Zhou, T.S., 1985. Characteristics of granitoids and their related metallogenesis in the Western Qinling. Northwestern Geol. 5, 6–15 (in Chinese).
Xiong, X., Zhu, L.M., Zhang, G.W., Li, B., Qi, L., Stevenson, D., Yang, T., Wang, F., Zheng, J., Jiang, H., Guo, A.L., 2016. Geology and geochemistry of the Triassic Wenquan Mo deposit and Mo-mineralized granite in the Western Qinling Orogen, China. Gondwana Res. 30, 159–178.
Yang, L.Q., Deng, J., Dilek, Y., Qiu, K.F., Ji, X.Z., Li, N., Taylor, R.D., Yu, J.Y., 2015a. Structure, geochronology, and petrogenesis of the Late Triassic Puziba granitoid dikes in the Mianlue suture zone, Qinling orogen, China. Geol. Soc. Am. Bull. 11 (12), 1831–1854.
Yang, L.Q., Deng, J., Qiu, K.F., Ji, X.Z., Santosh, M., Song, K.R., Song, Y.H., Geng, J.Z., Zhang, C., Hua, B., 2015b. Magma mixing and crust–mantle interaction in the Triassic monzogranites of Bikou Terrane, central China: constraints from petrology, geochemistry, and zircon U-Pb–Hf isotopic systematics. J. Asian Earth Sci. 98, 320–341.
Yang, L.Q., Deng, J., Wang, Z.L., Guo, L.N., Li, R.H., Groves, D.I., Danyushevskiy, L., Zhang, C., Zheng, X.L., Zhao, H., 2016. Relationships between gold and pyrite at the Xincheng gold deposit, Jiaodong Peninsula, China: implications for gold source and deposition in a brittle epizonal environment. Econ. Geol. 111, 105–126.
Zhang, H.F., Jin, L.L., Zhang, L., Harris, N., 2007. Geochemical and Pb-Sr-Nd isotopic compositions of granitoids from western Qinling belt: Constraints on basement nature and tectonic affinity. Sci. China (Series D): Earth Sci. 50, 184–196.
Zhang, J., Deng, J., Chen, H.Y., Yang, L.Q., Cooke, D., Danyushevsky, L., Gong, Q.J., 2014. LA-ICP-MS trace element analysis of pyrite from the Chang'an gold deposit, Sanjiang region, China: implication for ore-forming process. Gondwana Res. 26, 557–575.
Zheng, Y.F., 1993. Calculation of oxygen-isotope fractionation in hydroxyl-bearing silicates. Earth Planet. Sci. Lett. 120, 247–263.
Zhu, L.M., Ding, Z.J., Yao, S.Z., Zhang, G.W., Song, S.G., Qu, W.J., Guo, B., Li, B., 2009. Ore-forming event and geodynamic setting of molybdenum deposit at Wenquan in Gansu Province, Western Qinling. Chin. Sci. Bull. 54 (16), 2309–2324.
Zhu, L.M., Zhang, G.W., Chen, Y.J., Ding, Z.J., Guo, B., Wang, F., Lee, B., 2011. Zircon U-Pb ages and geochemistry of the Wenquan Mo-bearing granitioids in West Qinling, China: constraints on the geodynamic setting for the newly discovered Wenquan Mo deposit. Ore Geol. Rev. 39 (1–2), 46–62.